PHYSICAL REVIEW B **93**, 205132 (2016)

Ca_3P_2 and other topological semimetals with line nodes and drumhead surface states

Y.-H. Chan,[1] Ching-Kai Chiu,[2,3,4] M. Y. Chou,[1,5] and Andreas P. Schnyder[6,*]

[1]*Institute of Atomic and Molecular Sciences, Academia Sinica, Taipei 10617, Taiwan*

[2]*Department of Physics and Astronomy, University of British Columbia, Vancouver, British Columbia, Canada V6T 1Z1*

[3]*Quantum Matter Institute, University of British Columbia, Vancouver, British Columbia, Canada V6T 1Z4*

[4]*Condensed Matter Theory Center, Department of Physics, University of Maryland, College Park, Maryland 20742, USA*

[5]*School of Physics, Georgia Institute of Technology, Atlanta, Georgia 30332, USA*

[6]*Max-Planck-Institut für Festkörperforschung, Heisenbergstrasse 1, D-70569 Stuttgart, Germany*

(Received 28 October 2015; published 17 May 2016)

As opposed to ordinary metals, whose Fermi surfaces are two dimensional, topological (semi)metals can exhibit protected one-dimensional Fermi lines or zero-dimensional Fermi points, which arise due to an intricate interplay between symmetry and topology of the electronic wave functions. Here, we study how reflection symmetry, time-reversal symmetry, SU(2) spin-rotation symmetry, and inversion symmetry lead to the topological protection of line nodes in three-dimensional semimetals. We obtain the crystalline invariants that guarantee the stability of the line nodes in the bulk and show that a quantized Berry phase leads to the appearance of protected surfaces states, which take the shape of a drumhead. By deriving a relation between the crystalline invariants and the Berry phase, we establish a direct connection between the stability of the line nodes and the drumhead surface states. Furthermore, we show that the dispersion minimum of the drumhead state leads to a Van Hove singularity in the surface density of states, which can serve as an experimental fingerprint of the topological surface state. As a representative example of a topological semimetal, we consider Ca_3P_2, which has a line of Dirac nodes near the Fermi energy. The topological properties of Ca_3P_2 are discussed in terms of a low-energy effective theory and a tight-binding model, derived from *ab initio* DFT calculations. Our microscopic model for Ca_3P_2 shows that the drumhead surface states have a rather weak dispersion, which implies that correlation effects are enhanced at the surface of Ca_3P_2.

DOI: 10.1103/PhysRevB.93.205132

I. INTRODUCTION

The study of band structure topology of insulating and semimetallic materials has become an increasingly important topic in modern condensed matter physics [1–5]. The discovery of spin-orbit induced topological insulators has revealed that a nontrivial momentum-space topology of the electronic bands can give rise to new states of matter with exotic surface states [6–11] and highly unusual magnetotransport properties [12–14]. Recently, due to the experimental detection of arc surface states in Weyl semimetals [15], considerable attention has focused on the investigation of topological semimetals [16–30]. While in ordinary three-dimensional metals filled and empty states are separated by two-dimensional Fermi sheets, topological semimetals can exhibit zero-dimensional Fermi points or one-dimensional Fermi lines.

Classic examples of topological semimetals are the Weyl and Dirac semimetals which exhibit twofold and fourfold degenerate Fermi points, respectively. Weyl points can occur in the absence of any symmetry besides translation, whereas Dirac points are topologically stable only in the presence of time-reversal symmetry together with a crystal lattice symmetry, such as rotation or reflection. For example in the Dirac materials Cd_3As_2 [31–36] and Na_3Bi [37–41], the gapless property of the Dirac points is protected by a C_4 and C_3 crystal rotation symmetry, respectively. Correspondingly, the stability of Weyl points is guaranteed by a Chern number, while Dirac points are protected by a crystalline invariant, e.g., a mirror number [3]. Due to their topological characteristics these point-node semimetals display a number of exotic transport phenomena, such as negative magnetoresistance and chiral magnetic effect [24,42–45].

Probably even more interesting than semimetals with point nodes are topological materials with line nodes, since they support weakly dispersing surface states that could provide an interesting platform for exotic correlation physics [46–48]. Moreover, these semimetals are expected to exhibit long-range Coulomb interaction [49] and graphene-like Landau levels [50]. In nodal line semimetals the valence and conduction bands cross along one-dimensional lines in momentum space forming a ring-shaped nodal line. In general, this nodal line is not pinned at the Fermi energy, but passes through the Fermi energy at discrete points. As a consequence, the Fermi surface takes the shape of a thin tube with changing radius, possibly with constrictions. However, as we will see, for the case of Ca_3P_2 the band crossing occurs within ± 10 meV of the Fermi energy, leading to an approximate "Fermi line."

From the general classification of gapless topological materials [3] it follows that line nodes in semimetals are stable against gap opening only in the presence of a lattice symmetry, such as reflection [18–20]. That is, the two bands that cross at (or near) the Fermi level of a nodal line semimetal have opposite crystal symmetry eigenvalues, which prevents hybridization. For example, in noncentrosymmetric $PbTaSe_2$ [51,52] and $TlTaSe_2$ [53] the reflection about the Ta atomic planes protects the topological nodal lines. Similarly, the band crossings in Cu_3PdN [54], ZrSiS [55], Ca_3P_2 [56], and hyperhoneycomb structures [57,58] are protected by point group symmetries. Since the latter systems are symmetric under both inversion and time reversal, their nodal rings

*a.schnyder@fkf.mpg.de

are fourfold degenerate, i.e., of "Dirac type." In contrast, $PbTaSe_2$ and $TlTaSe_2$ lack inversion symmetry and hence exhibit "Weyl rings," which are only twofold degenerate. Among the aforementioned compounds only Ca_3P_2 has line nodes that are at the Fermi energy. Therefore, Ca_3P_2 is an ideal system to study unconventional transport properties of nodal line semimetals, since it is not necessary to tune the Fermi energy to the Dirac line by gating or doping.

In this paper, we discuss the stability of topological nodal lines in terms of crystalline topological invariants that take on nonzero quantized values. These topological numbers measure the global phase structure of the electronic wave functions in the presence of symmetry constraints. We derive and compute the $\mathbb{Z}$- and $\mathbb{Z}_2$-type crystalline invariants for systems with reflection symmetry and/or inversion symmetry. It follows from our analysis that fourfold degenerate Dirac rings are protected against gap opening by SU(2) spin-rotation symmetry and reflection symmetry or the product of time-reversal with inversion symmetry. These Dirac rings can be split into two twofold degenerate Weyl rings by spin-rotation symmetry breaking perturbations.

Unlike in crystalline topological insulators [59–63], the $\mathbb{Z}$-type crystalline invariants for nodal line semimetals are not directly linked with the appearance of surface states. Nevertheless, as we show in Sec. II C there appear topological in-gap states at the surface of nodal line semimetals, which arise from a quantized Berry phase (i.e., a $\mathbb{Z}_2$-type invariant), rather than the $\mathbb{Z}$-type crystalline invariant. Since the Berry phase is equal to π for any closed path that interlinks with the nodal line, surface states occur within two-dimensional regions of the surface Brillouin zone. These surface states take the form of a drumhead that is bounded by the projected nodal lines (Fig. 3). We derive in Sec. II D an important relation [Eq. (2.11)] between the $\mathbb{Z}$-type mirror invariant and the Berry phase, which establishes a direct connection between the appearance of the drumhead surface state and the topological stability of the bulk nodal line. It follows from this relation that drumhead boundary states are a generic feature of topological nodal line semimetals, occurring in both Weyl and Dirac ring systems (cf. Figs. 3, 5, and 6). We find that the drumhead surface state exhibits in general a Van Hove singularity in its dispersion, which gives rise to a kink in the surface density of states. The latter can be used as an experimental fingerprint of drumhead surface states [cf. Fig. 3(c)].

To illustrate the aforementioned properties of topological nodal line semimetals, we consider Ca_3P_2 as a representative example. We construct a tight-binding and low-energy continuum description of Ca_3P_2 and use these low-energy theories to compute the $\mathbb{Z}$- and $\mathbb{Z}_2$-type crystalline invariants of this material. It is shown that the drumhead surface state of Ca_3P_2 has a surprisingly weak dispersion, with an effective mass of about four times the bare electron mass. The latter implies that correlation effects are enhanced, which may lead to exotic symmetry-broken states at the surface of Ca_3P_2. The low-energy descriptions of Ca_3P_2, which we derive in Secs. II and III, will be of use for future theoretical studies on the electric- and magneto-transport properties of line node semimetals.

In the presence of disorder or interactions the surface states of nodal line semimetals can scatter and interact with quasiparticles in the bulk, since there is no full gap in the system. Hence, impurity scattering or electron-electron correlations might potentially destroy the boundary modes. For the nearly flat surface states of Ca_3P_2 the effects of interactions are particularly strong, since their large density of states enhances correlation effects. Hence, even relatively weak interactions may lead to exotic symmetry broken states at the surface, such as surface magnetism or surface superconductivity. Regarding the effects of disorder, we find that bulk impurities do not destroy the surface states as long as (i) the disorder strength is considerably smaller than the energy gap separating valence from conduction bands and (ii) the disorder respects reflection symmetry on average (Sec. IV).

The remainder of this paper is organized as follows. In Sec. II we discuss the topological features of nodal line semimetals in terms of a tight-binding model. We start in Sec. II A by deriving a twelve-band tight-binding Hamiltonian for Ca_3P_2 using maximally localized Wannier functions. This is followed by a discussion of the topological stability of the Dirac ring in Sec. II B. We show in Sec. II C that a nonzero quantized Berry phase leads to the appearance of nearly flat surface states. The relation between the Berry phase and the crystalline topological invariant is derived in Sec. II D. Section II E is devoted to the study of time-reversal and inversion breaking perturbations, which split the Dirac ring into two Weyl rings. To show that the topological features discussed in Sec. II are generic to any nodal line semimetal, we discuss in Sec. III an effective continuum model that describes the low-energy physics near a general topological nodal line. We evaluate the crystalline invariant for this continuum model in Sec. III A. In Sec. III B we study how time-reversal and inversion breaking terms split the nodal line. Finally, in Sec. IV we conclude the paper and give an outlook on future research. Section IV also contains a brief discussion of the effects of disorder on the topological surface states. Some technical details have been relegated to four Appendices.

II. TIGHT-BINDING CALCULATIONS

In this section, we examine the band structure topology of Ca_3P_2 in terms of a tight-binding model with twelve bands. Although the analysis below is performed specifically for Ca_3P_2, the principles discussed in this section are valid more generally and can be applied to any material with the same symmetries as Ca_3P_2.

A. Tight-binding model for Ca_3P_2

Recently, a new polymorph of Ca_3P_2 has been synthesized which crystallizes in a hexagonal lattice structure with space group $P6_3/mcm$ [56]. Figures 1(a) and 1(b) display the crystal structure of this polymorph of Ca_3P_2, which contains two layers with three Ca and three P atoms separated by four interstitial Ca atoms. High-resolution x-ray diffraction measurements [56] show that the Ca site is only partially occupied, yielding a Ca^{2+}-P^{3-} charge-balanced compound.

To determine the electronic band structure we perform first-principles calculations with the WIEN2k code [64] using as an input the experimental crystal structure of Ref. [56]. For the exchange-correlation functional we choose the generalized-gradient approximation of Perdew-Burke-Ernzerhof type [65].

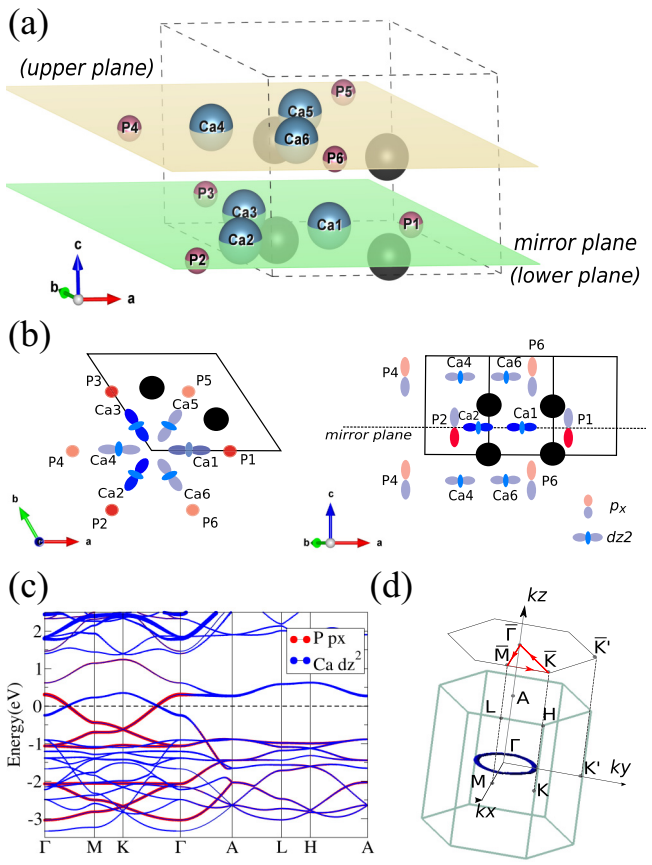

FIG. 1. Crystal structure and electronic bands of Ca_3P_2. (a) Crystal structure of Ca_3P_2, which contains two planes with three Ca atoms (blue) and three P atoms (red) that are separated by interstitial Ca atoms (black). The gray dashed lines indicate the unit cell. (b) Top and side view of the crystal structure. The P-p_x and Ca-d_{z^2} orbitals included in the tight-binding model are shown schematically. (c) Calculated electronic band structure of Ca_3P_2. The weights of the P-p_x and Ca-d_{z^2} orbitals that are located within the layers are indicated by the width of the corresponding band. The weight of the Ca-d_{z^2} orbital is multiplied by 2 to make it more visible on the scale of the plot. (d) Fermi ring of Ca_3P_2 as obtained from the tight-binding model, Eq. (2.2). The bulk and surface Brillouin zones are outlined by the green and black lines, respectively.

The full Brillouin zone is sampled by $21\times21\times22$ k points and the plane-wave cutoff is set to $RK_{\max} = 7$. We take the partial occupancy of the Ca sites into account by using the virtual crystal approximation [66]. Within this approximation the partial occupancy is included in an effective way, by lowering the valence of Ca atoms and adjusting the core charges accordingly. This approximation allows us to circumvent the use of large supercells, which would be computationally too costly. Figure 1(c) shows the calculated band structure of Ca_3P_2 within an energy range of ±3 eV around the Fermi energy E_F. To obtain the orbital character of the bands we introduce a local coordinate system for each Ca and P site, whose definition is illustrated in Fig. 1(b). In each coordinate frame the x axis is oriented along the c direction, whereas the z axis lies with the ab plane, pointing towards the lower left edge of the unit cell. With these definitions, we find that the bands close to the Fermi energy mainly originate from the Ca-d_{z^2} and P-p_x orbitals that are located within the layers [Fig. 1(c)]. The other orbitals of the in-plane atoms (Ca-d_{xy}, Ca-d_{xz}, Ca-d_{yz}, Ca-$d_{x^2-y^2}$, P-p_y, and P-p_z), as well as all the orbitals of the Ca interstitials, contribute insignificantly to the low-energy bands and can be neglected for the construction of the tight-binding model.

Guided by these observations, we use the six Ca-d_{z^2} and the six P-p_x orbitals that are located within the two layers as a basis set for the low-energy tight-binding model. Hence, the tight-binding Hamiltonian is defined in terms of a twelve-component Bloch spinor

$$\left|\psi^{\alpha}_{\mathbf{k}}\right\rangle = \frac{1}{\sqrt{N}}\sum_{\mathbf{R}} e^{i\mathbf{k}\cdot(\mathbf{R}+\mathbf{s}_\alpha)}\left|\phi^{\alpha}_{\mathbf{R}}\right\rangle, \tag{2.1}$$

where α is the orbital index, $\mathbf{R}$ denotes the lattice vectors, and $\mathbf{s}_\alpha$ represents the position vectors of the six Ca ($\alpha = 1,\ldots,6$) and the six P sites ($\alpha = 7,\ldots,12$), as specified in Figs. 1(a) and 1(b). For completeness, the numerical values of the position vectors $\mathbf{s}_\alpha$ are given in Table I of Appendix A. At this stage of the discussion, we ignore the spin degree of freedom of the Bloch spinor, since spin-orbit coupling is negligibly small for the light elements Ca and P. Using the spinor (2.1), we construct the matrix elements of the Bloch Hamiltonian as

$$H^{\alpha\beta}(\mathbf{k}) = \left\langle\psi^{\alpha}_{\mathbf{k}}\right|H\left|\psi^{\beta}_{\mathbf{k}}\right\rangle = \sum_{\mathbf{R}} e^{i\mathbf{k}\cdot(\mathbf{R}+\mathbf{s}_\alpha-\mathbf{s}_\beta)} t^{\alpha\beta}_{\mathbf{R}}, \tag{2.2}$$

where $t^{\alpha\beta}_{\mathbf{R}}$ is the hopping amplitude from orbital α in the unit cell at the origin to orbital β in the unit cell at position $\mathbf{R}$. To simplify the form of the matrix elements (2.2) and to obtain a single-valued Hamiltonian, we absorb a momentum-dependent phase factor in the definition of the basis orbitals; i.e., we let $|\psi^{\alpha}_{\mathbf{k}}\rangle \to e^{i\mathbf{k}\cdot\mathbf{s}_\alpha}|\psi^{\alpha}_{\mathbf{k}}\rangle$. We observe that Hamiltonian (2.2) has a nested block structure

$$H(\mathbf{k}) = \begin{pmatrix} \mathrm{H_{CaCa}} & \mathrm{H_{CaP}} \\ \mathrm{H_{PCa}} & \mathrm{H_{PP}} \end{pmatrix}, \quad H_{ij} = \begin{pmatrix} h^{\mathrm{ll}}_{ij} & h^{\mathrm{lu}}_{ij} \\ h^{\mathrm{ul}}_{ij} & h^{\mathrm{uu}}_{ij} \end{pmatrix}, \tag{2.3}$$

where the subblocks h^{mn}_{ij} with fixed $i,j \in \{\mathrm{Ca,P}\}$ and fixed $m,n \in \{\mathrm{l,u}\}$ are 3×3 matrices. The outer blocks H_{ij} represent hopping processes among and between the Ca and P orbitals, whereas the inner blocks $(h^{\mathrm{uu}}_{ij}, h^{\mathrm{ll}}_{ij})$ and $(h^{\mathrm{lu}}_{ij}, h^{\mathrm{ul}}_{ij})$ describe intralayer and interlayer hoppings, respectively. The detailed form of the matrix elements h^{mn}_{ij} is specified in Appendix A 1, where we also describe how the hopping parameter values are determined from a maximally localized Wannier function (MLWF) method [67,68].

In Fig. 1(d) we plot the energy isosurface of Hamiltonian (2.2) at $E = E_F \pm 20$ meV, which shows that the tight-binding model correctly captures the fourfold degenerate Dirac ring of Ca_3P_2. Comparing the first-principles band structure of Fig. 1(c) with the tight-binding bands displayed in Fig. 2, we find that the tight-binding model closely reproduces the bands with dominant Ca-d_{z^2} and P-p_x orbital character. In particular, the linear dispersion close to the Dirac ring agrees well with the first-principles results.

1. Symmetries

As we will see in the following sections, time-reversal, inversion, reflection, and SU(2) spin-rotation symmetry play

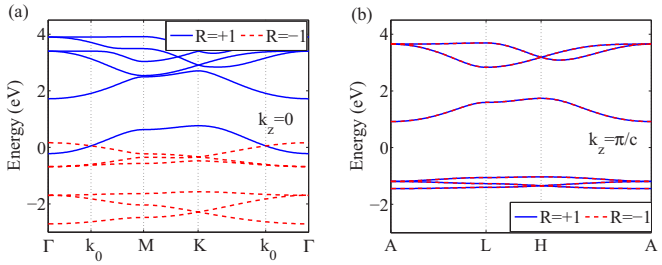

FIG. 2. Band structure of the tight-binding model. Panels (a) and (b) show the energy bands of Hamiltonian (2.2) along high-symmetry lines within the mirror planes $k_z = 0$ and $k_z = \pi/c$, respectively [cf. Fig. 1(d)]. The reflection eigenvalues of the bands are indicated by color, with blue and red corresponding to $R = +1$ and $R = -1$, respectively.

a crucial role for the protection of the Dirac ring. Let us therefore discuss how these symmetries act on the tight-binding Hamiltonian.

First of all, since we did not include the spin degree of freedom in Eq. (2.2), the tight-binding model is fully SU(2) spin-rotation invariant. That is, our model is diagonal in spin space with Hamiltonian (2.2) representing the diagonal element. As a consequence, the time-reversal operator is simply given by the identity matrix times the complex conjugation operator $\mathcal{K}$, i.e., $T = \mathbb{1}\mathcal{K}$, which acts on the Hamiltonian as

$$T^{-1}H(-\mathbf{k})T = H(\mathbf{k}). \tag{2.4}$$

Hence, Hamiltonian (2.2) belongs to symmetry class AI, since $T^2 = +1$. According to the classification of Ref. [3] Fermi rings in this symmetry class are unstable in the absence of lattice symmetries. However, as we will discuss below, reflection symmetry or a combination of inversion with time-reversal symmetry can produce a topological protection of the Dirac ring.

The two layers of the crystal structure of Ca_3P_2, indicated in green and brown in Fig. 1(a), are reflection planes. For brevity, we only discuss the lower reflection plane [colored in green in Fig. 1(a)], but the following analysis also holds, *mutatis mutandis*, for the upper plane. The invariance of the tight-binding Hamiltonian (2.2) under reflection about the lower plane implies

$$R^{-1}(k_z)H(k_x,k_y,-k_z)R(k_z) = H(k_x,k_y,k_z), \tag{2.5a}$$

with the k_z-dependent reflection operator

$$\begin{aligned} R(k_z) &= \tau_z \otimes e^{i\frac{k_z}{2}(\rho_z-\rho_0)c} \otimes \mathbb{1}_{3\times3} \\ &= \tau_z \otimes \begin{pmatrix} 1 & 0 \\ 0 & e^{+ik_zc} \end{pmatrix} \otimes \mathbb{1}_{3\times3}, \end{aligned} \tag{2.5b}$$

where c is the length of the lattice vector along the (001) direction. Here, the two sets of Pauli matrices τ_α and ρ_α describe the orbital (Ca-d_{z^2}, P-p_x) and the layer (l,u) degrees of freedom, respectively. The form of the reflection operator $R(k_z)$ follows from the observations that (i) the P-p_x orbitals are odd under reflection, while the Ca-d_{z^2} orbitals are even; and (ii) the mirror symmetry maps the orbitals in the upper layer to the next unit cell, which gives rise to the phase factor e^{+ik_zc}. Finally, we find that the tight-binding model is also inversion symmetric. That is, Hamiltonian (2.2) satisfies

$$I^{-1}H(-\mathbf{k})I = H(\mathbf{k}), \tag{2.6}$$

with the spatial inversion operator $I = \tau_0 \otimes \rho_x \otimes \mathbb{1}_{3\times3}$.

B. Topological protection of the Fermi ring

Let us now discuss how reflection symmetry (2.5) leads to the topological protection of the Dirac ring. First, we observe that for $\mathbf{k}$ within the reflection plane $k_z = 0,\pi$ the mirror operator $R(k_z)$ commutes with Hamiltonian (2.2), i.e., $[R(k_z),H(k_x,k_y,k_z)] = 0$ for $k_z = 0,\pi$. Therefore, it is possible to block-diagonalize $H(\mathbf{k})$ within the mirror planes with respect to R. In this block-diagonal basis each eigenstate of $H(\mathbf{k})$ has either mirror eigenvalue $R = +1$ or $R = -1$. As we can see from Fig. 2(a), the two bands that cross at the Dirac point have opposite mirror eigenvalues, which prevent hybridization between them. In other words, any term that couples the two bands breaks reflection symmetry. The stability of the band crossing is guaranteed by a mirror invariant of type $M\mathbb{Z}$ [18]. This mirror index is given by the difference of occupied states with eigenvalue $R = +1$ on either side of the Dirac ring, i.e.,

$$N^0_{M\mathbb{Z}} = n^{+,0}_{\text{occ}}(|\mathbf{k}_\parallel| > k_0) - n^{+,0}_{\text{occ}}(|\mathbf{k}_\parallel| < k_0), \tag{2.7}$$

where $\mathbf{k}_\parallel = (k_x,k_y)$ is the in-plane momentum and $n^{+,0}_{\text{occ}}(\mathbf{k}_\parallel)$ denotes the number of occupied states at $(\mathbf{k}_\parallel,0)$ in the mirror eigenspace $R = +1$. For the discussed nodal line semimetal we find that

$$n^{+,0}_{\text{occ}}(\mathbf{k}_\parallel) = \begin{cases} 1, & |\mathbf{k}_\parallel| < k_0 \ \text{(inside the ring)}, \\ 0, & |\mathbf{k}_\parallel| > k_0 \ \text{(outside the ring)}. \end{cases} \tag{2.8}$$

For a topological nodal line semimetal the mirror index $N^0_{M\mathbb{Z}}$ evaluates always to -1. For a nontopological semimetal, however, this index is zero.

In passing, we note that Hamiltonian (2.2) is a member of symmetry class AI with R_+ in the terminology of Ref. [18], since $T^2 = +1$ and R commutes with T. However, nodal lines with codimension $p = 2$ in class AI with R_+ are unstable, since for this class there does not exist any zero-dimensional invariant defined at time-reversal invariant momenta within the mirror plane. Nevertheless, the Dirac band crossing is protected, since the Hamiltonian can also be viewed as a member of class A with R. The mirror invariant for the latter class [i.e., Eq. (2.8)], which is defined for any in-plane momentum $\mathbf{k}_\parallel$, can be nonzero even in the presence of time-reversal symmetry. Besides reflection symmetry, the product of inversion and time-reversal symmetry IT also protects the Dirac line. This will be discussed at the end of Sec. II C and in Sec. III B 1 in terms of a low-energy continuum model.

C. Surface states and Berry phase

In this section, we present the surface spectrum of Ca_3P_2 as obtained from the tight-binding model (2.2) and show that, due to a nonzero Berry phase, there appear nearly flat ingap states at the surface. Figure 3(a) displays the surface band structure for the (001) surface in a three-dimensional slab geometry with 60 unit cells. The surface momentum is varied along a high-symmetry path, which is drawn in red in the

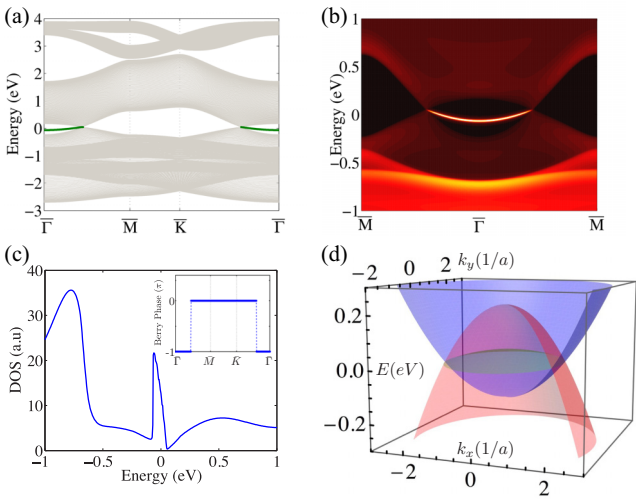

FIG. 3. Drumhead surface states and Berry phase. (a) Surface band structure of Ca_3P_2 as obtained from the tight-binding model (2.2) for the (001) surface in slab geometry with 60 unit cells. The surface state is highlighted in green. (b) Momentum-resolved surface density of states of Hamiltonian (2.2) for the (001) surface. White and dark red correspond to high and low density, respectively. (c) Energy-resolved surface density of states. The dispersion minimum of the drumhead state gives rise to a Van Hove singularity, i.e., a kink at $E = -0.06$ eV. The inset shows the variation of the Berry phase (2.9) of Hamiltonian (2.2) along high-symmetry lines of the (001) surface Brillouin zone [see Fig. 1(d)]. (d) Surface spectrum of the low-energy effective model (3.1) for the (001) face as a function of surface momenta k_x and k_y. The bulk states at $k_z = 0$ with reflection eigenvalues $R = +1$ and $R = -1$ are colored in blue and red, respectively. The drumhead surface state is indicated by the green area.

surface Brillouin zone of Fig. 1(d). Using an iterative Green's function method [69] we compute the momentum-resolved surface density of states for a semi-infinite (001) slab, which is shown in Fig. 3(b). As indicated by the green area in Fig. 3(d) and by the green and yellow lines in Figs. 3(a) and 3(b), respectively, the surface state is nearly dispersionless, taking the shape of a drumhead that is bounded by the projected Dirac ring. The dispersion minimum of this drumhead state gives rise to a Van Hove singularity at $E = -0.06$ eV, which leads to kink in the surface density of states. This is visible in Fig. 3(c) as a jump in the surface density of states as the Fermi energy is approached from below. The existence of a drumhead surface state with a Van Hove singularity is not limited to Ca_3P_2, but is valid more generally, for any topological nodal line semimetal with reflection symmetry or inversion plus time-reversal symmetry. We note that nearly or completely flat surface states have recently also been studied in photonic crystals [70], in noncentrosymmetric superconductors [71–74], in bernal graphite [75], and in topological crystalline insulator heterostructures [47].

In contrast to crystalline topological insulators the surface states of the semimetal (2.2) are not directly related to the mirror invariant (2.7), but are connected to a nonzero Berry phase. To make this connection explicit, we decompose the (001) slab considered in Fig. 3 into a family of one-dimensional systems parametrized by the in-plane momentum $\mathbf{k}_\parallel = (k_x, k_y)$. For fixed $\mathbf{k}_\parallel$, the Berry phase is defined as

$$\mathcal{P}(\mathbf{k}_\parallel) = -i \sum_{E_j < E_F} \int_{-\pi}^{\pi} \langle u_j(\mathbf{k}) | \partial_{k_z} | u_j(\mathbf{k}) \rangle dk_z, \tag{2.9}$$

where the sum is over filled Bloch eigenstates $|u_j(\mathbf{k})\rangle$ of Hamiltonian (2.2). As was shown by King-Smith and Vanderbilt [76], the Berry phase $\mathcal{P}(\mathbf{k}_\parallel)$ is related to the charge q_{end} at the end of the one-dimensional system with fixed in-plane momentum $\mathbf{k}_\parallel$, i.e.,

$$q_{\text{end}} = \frac{e}{2\pi} \mathcal{P}(\mathbf{k}_\parallel) \mod e. \tag{2.10}$$

Hence, when $\mathcal{P}(\mathbf{k}_\parallel) \neq 0$ an in-gap state appears at $\mathbf{k}_\parallel$ in the surface Brillouin zone. For the tight-binding Hamiltonian (2.2) we find that there are two different symmetries which each quantize the Berry phase (2.9) to 0 or π, namely, the reflection symmetry (2.5) and the product of time-reversal and inversion symmetry IT; see Appendix B. In the inset of Fig. 3(c) we numerically compute $\mathcal{P}(\mathbf{k}_\parallel)$ using the tight-binding wave functions of Hamiltonian (2.2). We obtain that the Berry phase equals π for $\mathbf{k}_\parallel$ inside the projected Dirac ring, while it is zero for $\mathbf{k}_\parallel$ outside the ring. This indicates that surface states occur within the projected Dirac ring, which is in agreement with the surface spectrum of Figs. 3(a) and 3(b). The Berry phase is defined modulo 2π, since large gauge transformations of the wave functions change it by 2π. As a result, $\mathcal{P}$ protects only single, but not multiple, surface states at a given $\mathbf{k}_\parallel$.

Remarkably due to the IT symmetry, the Berry phase $\mathcal{P}$ along any closed loop in the three-dimensional Brillouin zone is quantized (see Appendix B). This allows us to interpret the Berry phase as a topological invariant which guarantees the stability of the Dirac line in the presence of the IT symmetry. That is, for a loop interlinking with the Dirac ring, we find that $\mathcal{P} = \pm\pi$ which shows that the Dirac band crossing is protected by the product of inversion with time-reversal symmetry. The Berry phase represents a $\mathbb{Z}_2$-type invariant, since it is defined only up to multiples of 2π. In contrast, the mirror number (2.7) is a $\mathbb{Z}$-type invariant, which can take on any integer number. Therefore, only the mirror invariant $N_{M\mathbb{Z}}$ can give rise to the stability of multiple Dirac lines at the same location in the Brillouin zone.

D. Relation between Berry phase and mirror invariant

The analysis of the previous section suggests that the topological stability of the Dirac ring is closely related to the appearance of surface states. In order to put this connection on a firmer footing, we present here a relation between the mirror invariant and the Berry phase $\mathcal{P}(\mathbf{k}_\parallel)$. Namely, we find that

$$(-1)^{n_{\text{occ}}^{+,0}(\mathbf{k}_\parallel) + n_{\text{occ}}^{+,\pi}(\mathbf{k}_\parallel)} e^{i\partial R} = e^{i\mathcal{P}(\mathbf{k}_\parallel)} \tag{2.11a}$$

for all in-plane momenta $\mathbf{k}_\parallel = (k_x, k_y)$, where

$$\partial R = i \sum_{E_j < E_F} \int_0^{\pi} \langle u_j(\mathbf{k}) | R^\dagger(k_z) [\partial_{k_z} R(k_z)] | u_j(\mathbf{k}) \rangle dk_z \tag{2.11b}$$

denotes the change in phase of the reflection operator $R(k_z)$ along the reflection direction k_z. The invariants $n_{\text{occ}}^{+,0}(\mathbf{k}_\parallel)$ and $n_{\text{occ}}^{+,\pi}(\mathbf{k}_\parallel)$ correspond to the number of occupied states at $(\mathbf{k}_\parallel, 0)$

and $(\mathbf{k}_\parallel,\pi)$, respectively, with mirror eigenvalue $R=+1$. Formula (2.11), whose proof is derived in Appendix B, is one of the main results of this paper. For concreteness we have assumed in (2.11) that reflection symmetry $R(k_z)$ maps z to $-z$. But relation (2.11) is valid more generally, i.e., for any reflection-symmetric semimetal, in particular also for line node materials with strong spin-orbit coupling, such as $PbTaSe_2$ [51,52].

We observe that in general the reflection operator only depends on the momentum along the reflection direction [i.e., on k_z in the case of Eq. (2.5)], but is independent of the in-plane momenta $\mathbf{k}_\parallel$. Hence, we infer from Eq. (2.11) that when the mirror invariant $n^{+,0}_{\rm occ}(\mathbf{k}_\parallel)$ [or $n^{+,\pi}_{\rm occ}(\mathbf{k}_\parallel)$] changes by 1 as the in-plane momentum $\mathbf{k}_\parallel$ is moved across the topological Dirac line, the Berry phase increases by π, since ∂R does not depend on $\mathbf{k}_\parallel$. As a consequence, a drumhead surface state appears either inside or outside the projected Dirac ring. This proofs the direct connection between the stability of the Dirac ring and the existence of drumhead surface states. For the tight-binding model of Ca_3P_2, Eq. (2.2), we find that the phase change ∂R of the reflection operator (2.5) evaluates to 3π independent of $\mathbf{k}_\parallel$. Figure 2(b) shows that the number of occupied states with momentum $(\mathbf{k}_\parallel,\pi)$ and mirror eigenvalue $R=+1$ is $n^{+,\pi}_{\rm occ}(\mathbf{k}_\parallel)=3$ for all $\mathbf{k}_\parallel$. Using relation (2.11) together with Eq. (2.8), it follows that the Berry phase $\mathcal{P}$ equals π inside and 0 outside the Dirac ring, which agrees with the explicit calculation of $\mathcal{P}$; see inset of Fig. 3(c).

In closing this section, we note that for certain highly symmetric lattice models [61,77] the reflection operator R is completely momentum independent, in which case formula (2.11) simplifies to

$$\left[n^{+,0}_{\rm occ}(\mathbf{k}_\parallel)+n^{+,\pi}_{\rm occ}(\mathbf{k}_\parallel)\right]\pi=\mathcal{P}(\mathbf{k}_\parallel)\ (\mathrm{mod}\ 2\pi), \qquad (2.12)$$

for all $\mathbf{k}_\parallel$ [78]. Hence, in this case the Berry phase, and therefore the location of the surface states, is fully determined by the mirror invariant (2.8). This is useful, since the mirror number (2.8) is easier to compute than the Berry phase, for which one needs to determine the momentum dependence of the tight-binding wave functions.

E. Symmetry-breaking perturbations

We have seen that the stability of the Dirac ring of Ca_3P_2 is protected by SU(2) spin-rotation symmetry, reflection symmetry, and the product of inversion and time-reversal symmetry IT. In this section, we study how the breaking of these symmetries modifies the bulk and surface spectrum of Ca_3P_2.

1. Reflection and time-reversal symmetry breaking

First, we consider a reflection and time-reversal breaking perturbation with the following nonzero matrix elements:

$$\left\langle\psi^1_{\mathbf{k}}\middle|H\middle|\psi^9_{\mathbf{k}}\right\rangle=+0.2\sin(\mathbf{k}\cdot\mathbf{r}_0) \qquad (2.13a)$$

and

$$\left\langle\psi^4_{\mathbf{k}}\middle|H\middle|\psi^{12}_{\mathbf{k}}\right\rangle=-0.2\sin(\mathbf{k}\cdot\mathbf{r}_0), \qquad (2.13b)$$

where $\mathbf{r}_0=(0.5,0.5,0)$ is a vector within the reflection plane along the diagonal direction. This term is odd in momentum $\mathbf{k}$

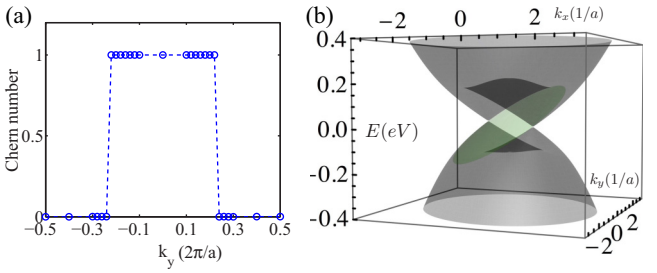

FIG. 4. Arc surface state and spin Chern number. (a) k_y dependence of the spin Chern number (2.14) of Hamiltonian (2.2) in the presence of the mirror and time-reversal symmetry breaking perturbation (2.13). (b) Surface and bulk spectra of the low-energy model (3.1) perturbed by the mass term (3.2) with $d=0.9$ eVÅ and $\theta_0=-\pi/4$, which breaks reflection and time-reversal symmetry. The bulk states and the arc state at the (001) surface are indicated in gray and green, respectively.

and couples the d_{z^2} orbitals at the Ca1 and Ca4 sites with the p_x orbitals at the P3 and P6 sites [cf. Figs. 1(a) and 1(b)]. It follows from Eqs. (2.5) and (2.6) that perturbation (2.13) breaks reflection and time-reversal symmetry, but respects inversion symmetry. Therefore, Eq. (2.13) gaps out the Dirac ring except for two points along the diagonal direction $(1,-1,0)$, where it vanishes [see Fig. 4(b)]. These two gap closing points are Dirac nodes (or Weyl nodes, if one disregards the spin degree of freedom), whose stability is guaranteed by the spin Chern number [79]

$$C_{\rm s}(k_y)=\frac{1}{2\pi i}\sum_{E_j<E_{\rm F}}\int_{T^2}\left[\partial_{k_x}A^{(j)}_z-\partial_{k_z}A^{(j)}_x\right]dk_x dk_z, \qquad (2.14)$$

where $A^{(j)}_\mu=\langle u_j|\partial_{k_\mu}|u_j\rangle$ is the Berry connection. We find that $C_{\rm s}(k_y)$ evaluates to $+1$ for k_xk_z planes in between the two Dirac points, while it is zero otherwise [Fig. 4(a)]. By the bulk-boundary correspondence, the nonzero spin Chern number (2.14) implies the appearance of an arc state in the surface Brillouin zone connecting the projections of the two Dirac nodes [green area in Fig. 4(b)]. As perturbation (2.13) is turned to zero, the arc state transforms into the drumhead surface state of Fig. 3.

2. Spin-rotation symmetry breaking

Second, we study the effects of SU(2) spin-rotation symmetry breaking induced, for example, by spin-orbit coupling. For Ca_3P_2 the spin-orbit interactions are negligible due to the small atomic number of Ca and P. However, there are a number of topological semimetals with heavy elements, such as $PbTaSe_2$ and $TlTaSe_2$, for which spin-orbit coupling is strong. Spin-orbit interactions can modify the energy spectrum of nodal line semimetals in two different ways: either they open up a full gap in the spectrum, or they split the Dirac ring into two Weyl rings. Here, we study the latter possibility. In order to do so, we need to explicitly include the spin degree of freedom in Hamiltonian (2.3); i.e., we consider

$$\hat{H}(\mathbf{k})=H(\mathbf{k})\otimes\sigma_0+\hat{H}_{\rm sb}(\mathbf{k}), \qquad (2.15)$$

where σ_0 operates in spin space and $\hat{H}_{\rm sb}$ represents a spin-rotation symmetry breaking term, which we specify below.

Time-reversal symmetry acts on $\hat{H}$ according to Eq. (2.4), but with the modified time-reversal operator $\hat{T} = T \otimes i\sigma_y$. Similarly, the reflection operator and the spatial inversion operator are changed to $\hat{R} = R \otimes \sigma_z$ and $\hat{I} = I \otimes \sigma_0$, respectively. To split the fourfold degenerate Dirac ring of Eq. (2.15) into two twofold degenerate Weyl rings, it is necessary to also break time-reversal or inversion symmetry, besides spin-rotation symmetry.

(a) *Time-reversal breaking perturbation*. The staggered Zeeman field

$$\hat{H}_{\rm sb}(\mathbf{k}) = h_z\, \tau_z \otimes \rho_0 \otimes \mathbb{1}_{3\times 3} \otimes \sigma_z \tag{2.16}$$

breaks both time-reversal and spin-rotation symmetry, but satisfies inversion and reflection symmetry. It describes an external staggered magnetic field with opposite signs on the Ca and P sites. According to the terminology of Ref. [18], Hamiltonian (2.15) perturbed by Eq. (2.16) is a member of class A with R, which exhibits an integer number of equivalence classes distinguished by a mirror invariant. In Figs. 5(a) and 5(c) we present the bulk energy bands of Hamiltonian (2.15) with an applied staggered Zeeman field of strength $h_z = 0.1$ eV. The bulk spectrum displays two Weyl rings, whose stability is guaranteed by the mirror number (2.7). Figures 5(b) and 5(d) show the surface energy spectrum at the (001) face. We find that there are two drumhead surface states which are bounded by the projections of the two Weyl rings. In accordance with the discussion of Secs. II C and II D [cf. Eq. (2.11)] the single surface state that appears between the projections of the outer and inner Weyl rings is protected by the Berry phase (2.9), which takes on the nonzero quantized value $\mathcal{P} = \pm\pi$. The two surface states that exist inside the projection of the inner Weyl ring, on the other hand, are topologically unstable.

(b) *Inversion-breaking perturbation*. To break inversion and spin-rotation symmetry we consider a perturbation with the following nonzero matrix elements:

$$\left\langle \psi^1_{\mathbf{k}\sigma} \middle| \hat{H} \middle| \psi^6_{\mathbf{k}\sigma} \right\rangle = +0.6i\ \mathrm{sgn}(\sigma) e^{i\mathbf{k}\cdot(\mathbf{s}_6 - \mathbf{s}_1)}[1 + e^{i\mathbf{k}\cdot\hat{\mathbf{e}}_z}] \tag{2.17a}$$

and

$$\left\langle \psi^7_{\mathbf{k}\sigma} \middle| \hat{H} \middle| \psi^{12}_{\mathbf{k}\sigma} \right\rangle = -0.3i\ \mathrm{sgn}(\sigma) e^{i\mathbf{k}\cdot(\mathbf{s}_{12} - \mathbf{s}_7 + \mathbf{R}_{110})}[1 + e^{i\mathbf{k}\cdot\hat{\mathbf{e}}_z}], \tag{2.17b}$$

where $|\psi^\alpha_{\mathbf{k}\sigma}\rangle$ denotes the Bloch spinor with orbital index α and spin index $\sigma = \pm$. The vectors $\mathbf{s}_\alpha$ are the position vectors of the atoms in the unit cell and are given in Table I of Appendix A. Perturbation (2.17) couples the orbitals at the Ca1 and P1 sites with the orbitals at the Ca6 and P6 sites, respectively. Using Eqs. (2.4), (2.5), and (2.6) one can check that the term (2.17) satisfies reflection and time-reversal symmetry, but breaks inversion symmetry. Since $\hat{T}^2 = -1$ and $\{\hat{T}, \hat{R}\} = 0$, Hamiltonian (2.15) perturbed by Eq. (2.17) is a member of class AII with R_- of Ref. [18], for which a mirror invariant can be defined. The bulk bands at $k_z = 0$ of Hamiltonian (2.15) in the presence of the inversion-breaking term (2.17)

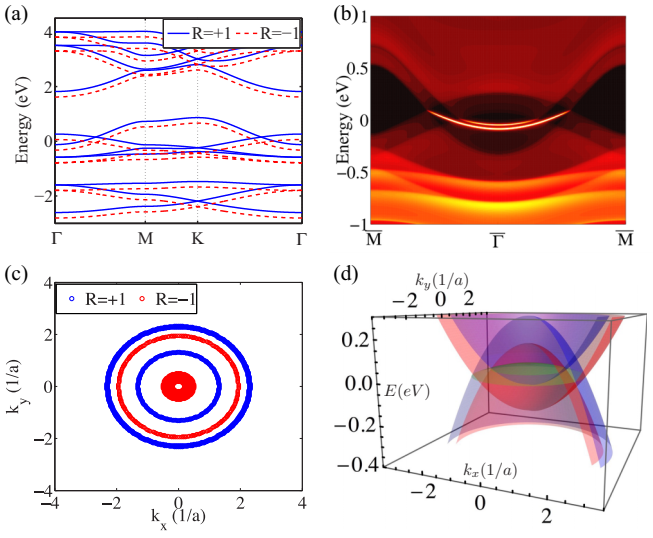

FIG. 5. Bulk bands and drumhead surface states of a spinful time-reversal breaking line node semimetal. Panels (a) and (b) show the bulk bands and the surface density of states of Hamiltonian (2.15) in the presence of the staggered Zeeman term (2.16) with $h_z = 0.1$ eV. The momentum in panel (a) is varied within the mirror plane $k_z = 0$ along high-symmetry lines of the Brillouin zone. (c) Energy isosurfaces of Hamiltonian (2.15) with $h_z = 0.1$ eV at $E_F \pm 5$ meV and $k_z = 0$. (d) Surface and bulk spectra of the low-energy effective model (3.3) perturbed by the time-reversal breaking term (3.4) with $v_\parallel h^z_{\rm eff} = 0.07$ eV. The drumhead states at the (001) surface are colored in green. The reflection eigenvalues of the bulk bands at $k_z = 0$ in panels (a), (c), and (d) are indicated by color, with blue and red corresponding to $R = +1$ and $R = -1$, respectively.

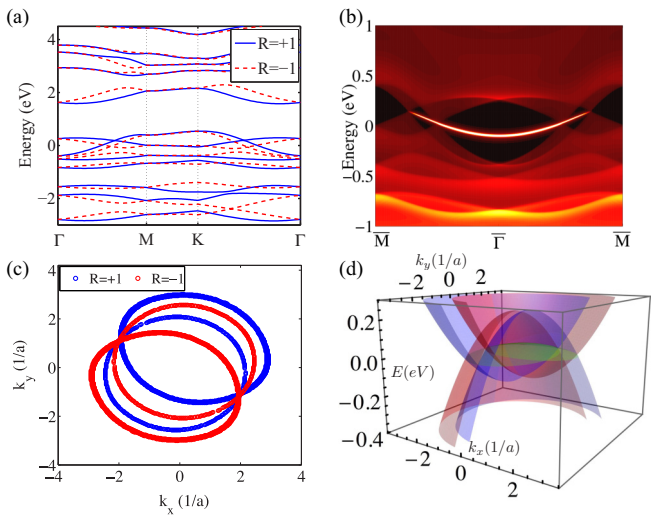

FIG. 6. Bulk bands and drumhead surface states of a spinful inversion-breaking line node semimetal. Panels (a) and (b) display the bulk bands and the surface density of states of tight-binding model (2.15) in the presence of the inversion-breaking term (2.17). The momentum in panel (a) is varied within the mirror plane $k_z = 0$ along high-symmetry lines. (c) Energy isosurfaces of Hamiltonian (2.15) perturbed by Eq. (2.17) at $E_F \pm 5$ meV and $k_z = 0$. (d) Surface and bulk spectra of the low-energy effective model (3.3) perturbed by the inversion-breaking term (3.6) with $\delta = 0.025$ eVÅ. The drumhead states at the (001) surface are indicated in green. The mirror eigenvalues of the bulk bands at $k_z = 0$ in panels (a), (c), and (d) are represented by color, with blue and red corresponding to $R = +1$ and $R = -1$, respectively.

are presented in Figs. 6(a) and 6(b). We observe that the Dirac ring is split into two Weyl rings, which intersect on the $(\sqrt{3}, -1, 0)$ axis. As in the previous cases, the Weyl nodal lines are protected by the nonzero mirror number (2.7). Figures 6(b) and 6(d) show the surface spectrum at the (001) surface, which exhibits two drumhead surface states. As before, we find that only the single surface state which occurs between the projections of the inner and outer rings is protected by the Berry phase (2.9).

III. LOW-ENERGY CONTINUUM THEORY OF NODAL LINE SEMIMETALS

In this section we present a low-energy effective theory for a general topological nodal line semimetal with time-reversal, reflection, and inversion symmetry. The form of this low-energy description is universal, since it is entirely dictated by symmetry. We start by discussing Dirac rings, which arise in semimetals with conserved SU(2) spin-rotation symmetry. Spin-rotation breaking semimetals with Weyl nodal lines will be discussed in Sec. III B 2.

Consider the following low-energy Hamiltonian with spin-rotation symmetry

$$H_{\text{eff}}(\mathbf{k}) = v_{\parallel}\left(k_{\parallel}^2 - k_0^2\right)\tau_z + v_z k_z \tau_y + f(\mathbf{k})\tau_0, \qquad (3.1)$$

which describes a Dirac ring within the $k_z = 0$ plane, located at $k_{\parallel}^2 := k_x^2 + k_y^2 = k_0^2$. In Eq. (3.1) we suppress the spin degree of freedom, since any spin-dependent terms are forbidden by symmetry. The Pauli matrices τ_i operate in orbital space and the function $f(\mathbf{k})$ is restricted by symmetry to be even in $\mathbf{k}$. We assume that $f(\mathbf{k}) = v_0(k_{\parallel}^2 - k_0^2) + V_0$, neglecting any terms of higher order in $\mathbf{k}$. To make a connection with the previous section, we fit the parameters $v_0, v_{\parallel}, v_z, k_0$, and V_0 to the low-energy band structure of the DFT calculations of Sec. II A [see Fig. 1(c)]. We find that the momentum parameter k_0 equals $k_0 = 0.206\,\text{Å}^{-1}$, the chemical potential is $V_0 = 0.095$ eV, and the velocities are given by $v_0 = -0.993$ eV Å^2, $v_{\parallel} = 4.34$ eV Å^2, and $v_z = 2.50$ eV Å. Employing Eqs. (2.4), (2.5), and (2.6), one can show that the low-energy Hamiltonian H_{eff} satisfies time-reversal, reflection, and inversion symmetry, with the symmetry operators $T_{\text{eff}} = \tau_0\mathcal{K}, R_{\text{eff}} = \tau_z$, and $I_{\text{eff}} = \tau_z$, respectively. Before we discuss in the next section the topological stability of the Dirac line (3.1), let us remark that $H_{\text{eff}}(\mathbf{k})$ can be converted in a straightforward manner to a lattice model; see Appendix C. In Figs. 3(d), 4(b), 5(d), and 6(d) we use the lattice version of Eq. (3.1) to plot the surface states. Observe that there are some minor differences in the shape of the surface states between the tight-binding model (2.2) and the effective theory (3.1) [compare Fig. 3(b) with Fig. 3(d)]. We attribute this difference to the omission of longer range hopping terms in Eq. (3.1).

A. Topological protection of the Fermi ring

As mentioned in Sec. II B, Dirac nodal lines are protected by either reflection symmetry R or the product of inversion with time-reversal symmetry IT. Let us now discuss this in terms of the low-energy theory (3.1).

(a) $\mathbb{Z}$ *classification due to reflection symmetry*. Considering only reflection symmetry and disregarding the spin degree of freedom, Hamiltonian (3.1) belongs to class A with R. Since the codimension of the Dirac ring is $p = 2$, it is classified by an $M\mathbb{Z}$ invariant (see Table II of Ref. [18]), i.e., by the mirror number (2.7), which measures the difference of occupied states with mirror eigenvalue $R_{\text{eff}} = +1$ on either side of the Dirac ring. The two bands that cross at the nodal line have opposite reflection eigenvalues, which prohibits hybridization between them. Indeed, we find that the hybridization term τ_x breaks reflection symmetry R_{eff}. We note that the mirror invariant (2.7) is of $\mathbb{Z}$ type and can therefore protect multiple Dirac crossings in the Brillouin zone. To verify this for the low-energy model (3.1), we enlarge the matrix dimension of Hamiltonian H_{eff} by considering $H_{\text{eff}} \otimes \mathbb{1}_{n\times n}$, which respects reflection symmetry with the enlarged reflection operator $R'_{\text{eff}} = R_{\text{eff}} \otimes \mathbb{1}_{n\times n}$. Hybridization terms for the enlarged Hamiltonian are of the form $\tau_x \otimes A$, with A an arbitrary $n \times n$ Hermitian matrix. However, since $(R'_{\text{eff}})^{-1}(\tau_x \otimes A)R'_{\text{eff}} = -\tau_x \otimes A$, all of these terms break reflection symmetry R'_{eff}.

(b) $\mathbb{Z}_2$ *classification due to IT symmetry*. Besides reflection, also the product of inversion with time-reversal symmetry $I_{\text{eff}}T_{\text{eff}}$ prohibits hybridization between the two bands, since the hybridization term τ_x is not invariant under $I_{\text{eff}}T_{\text{eff}} = \tau_z\mathcal{K}$. But in the presence of $I_{\text{eff}}T_{\text{eff}}$, Dirac nodal lines are classified as $\mathbb{Z}_2$ instead of $M\mathbb{Z}$. To see this, consider two copies of Hamiltonian H_{eff}, i.e., $H_{\text{eff}} \otimes \mu_0$, which satisfies IT symmetry with the doubled operator $I_{\text{eff}}T_{\text{eff}} \otimes \mu_0$. Here, μ_α denotes an additional set of Pauli matrices. The Dirac rings of this doubled Hamiltonian are topologically unstable, since the symmetry-preserving term $\tau_x \otimes \mu_y$ gaps out the nodal lines. As discussed at the end of Sec. II C, the product of inversion with time-reversal symmetry IT quantizes the Berry phase $\mathcal{P}$ to 0 or π [19,80]. Hence, $\mathcal{P}$ can be interpreted as a $\mathbb{Z}_2$ topological invariant that guarantees the stability of the nodal ring. In contrast to the mirror invariant, the integration path that enters in the definition of this $\mathbb{Z}_2$ number [cf. Eq. (2.9)] is not confined to the mirror plane. For any integration path that interlinks with the nodal line, $\mathcal{P} = \pm\pi$ signals the stability of the Dirac ring.

In closing we note that, while the low-energy theory (3.1) accurately captures the topological stability of the nodal ring of a given semimetal, it does not necessarily correctly reproduce the location of the drumhead surface state. That is, in order to determine whether the drumhead surface state is located inside or outside the projected Dirac ring, it is necessary to compute the Berry phase of all the occupied states. This information is not contained in the low-energy model (3.1); cf. Appendix C.

B. Symmetry-breaking perturbations

In analogy to the discussion of Sec. II E, we now study how different symmetry-breaking perturbations transform the Dirac ring (3.1) into Dirac points or Weyl rings.

1. Reflection and time-reversal symmetry breaking

The Dirac line node of H_{eff} can be deformed into two Dirac points by the perturbation

$$d\,\sin(\theta_{\parallel} - \theta_0)k_{\parallel}\tau_x, \qquad (3.2)$$

which breaks reflection and time-reversal symmetry, but respects inversion symmetry. Here, $\theta_\parallel = \tan^{-1}(k_y/k_x)$ and $k_\parallel = \sqrt{k_x^2 + k_y^2}$ denote polar angle and absolute value of the in-plane momentum $\mathbf{k}_\parallel$, respectively. The term (3.2) gaps the Dirac ring except at $\mathbf{k} = \pm k_0(\cos\theta_0, \sin\theta_0, 0)$. These two gap closing points are Dirac nodes with opposite chiralities, which are protected by the spin Chern number (2.14). Due to the bulk-boundary correspondence an arc state appears at the surface, connecting the projected Dirac points in the surface Brillouin zone. This is illustrated in Fig. 4(b), where we set $\theta_0 = -\pi/4$ and $d = 0.9$ eV Å, which mimics the effects of perturbation (2.13) for the tight-binding Hamiltonian (2.2).

From the arc surface state of the above Dirac semimetal one can infer the existence of the drumhead surface state of $H_{\rm eff}$, since the two transform into each other by letting d tend to zero in Eq. (3.2). Moreover, the one-dimensional set of Dirac nodes, induced by Eq. (3.2) and parametrized by θ_0, can be interpreted as the Dirac ring of $H_{\rm eff}$. That is, as we let θ_0 in Eq. (3.2) run from 0 to π a nodal ring is created. For each fixed θ_0 there is an arc surface state connecting the two points $\mathbf{k}_\parallel = \pm k_0(\cos\theta_0, \sin\theta_0)$ in the surface Brillouin zone. Hence, a drumhead surface state is generated when θ_0 is varied from 0 to π. From this argument one infers that drumhead states also appear at surfaces for which the Berry phase (2.9) is not quantized (cf. Sec. II C), since the appearance of arc states does not depend on any crystal symmetries.

2. *Spin-rotation symmetry breaking*

In the absence of SU(2) spin-rotation symmetry, the Dirac ring of $H_{\rm eff}$ is topologically unstable. To discuss this, we consider as in Sec. II E 2 a spinful version of Hamiltonian (3.1),

$$\hat{H}_{\rm eff}(\mathbf{k}) = \hat{H}_{\rm eff}(\mathbf{k}) \otimes \sigma_0 + \hat{H}^{\rm sb}_{\rm eff}(\mathbf{k}), \tag{3.3}$$

where the Pauli matrices σ_α describe the spin degree of freedom and $\hat{H}^{\rm sb}_{\rm eff}$ denotes a spin-rotation symmetry breaking term. $\hat{H}_{\rm eff}$ is invariant under the same symmetries as the spinful tight-binding Hamiltonian (2.15). That is, it satisfies time-reversal, reflection, and inversion symmetry with the operators $\hat{T} = \tau_0 \otimes i\sigma_y\mathcal{K}$, $\hat{R} = \tau_z \otimes \sigma_z$, and $\hat{I} = \tau_z \otimes \sigma_0$, respectively. We find that the Dirac nodal lines of $\hat{H}_{\rm eff}$ can be gapped out by the spin-rotation symmetry breaking mass terms $\tau_x \otimes \sigma_x$ and $\tau_x \otimes \sigma_y$, which preserve reflection symmetry $\hat{R}$ as well as $\hat{I}\hat{T}$ symmetry. These perturbations turn Hamiltonian (3.3) into a trivial insulator. However, there exist also other spin-rotation symmetry breaking terms that deform the Dirac ring into two Weyl rings. These perturbation terms break either time-reversal symmetry or inversion symmetry.

(a) *Time-reversal breaking perturbation*. First, we add a spin-rotation and time-reversal breaking term to the Hamiltonian $\hat{H}_{\rm eff}$, which takes the form of a staggered Zeeman field

$$\hat{H}^{\rm sb}_{\rm eff}(\mathbf{k}) = \nu_\parallel h^z_{\rm eff} \tau_z \otimes \sigma_z. \tag{3.4}$$

This perturbation respects reflection and inversion symmetry. It splits the Dirac ring into two Weyl rings that are located within the mirror plane $k_z = 0$ at $k_\parallel = \sqrt{k_0^2 \pm h^z_{\rm eff}}$. The stability of these Weyl nodal lines is guaranteed by the mirror invariant (2.7), which evaluates to

$$n^{+,0}_{\rm occ}(k_\parallel) = \begin{cases} 1, & k_\parallel < \sqrt{k_0^2 - h^z_{\rm eff}}, \\ 0, & \sqrt{k_0^2 - h^z_{\rm eff}} < k_\parallel < \sqrt{k_0^2 + h^z_{\rm eff}}, \\ 1, & \sqrt{k_0^2 + h^z_{\rm eff}} < k_\parallel. \end{cases} \tag{3.5}$$

In Fig. 5(d) we plot the surface spectrum of $H_{\rm eff}$ in the presence of the staggered Zeeman term with $\nu_\parallel h^z_{\rm eff} = 0.07$ eV. There appear two drumhead surface states which are bounded by the two projected Weyl rings.

(b) *Inversion-breaking perturbation*. Alternatively, the Dirac ring can be split into Weyl rings by an inversion-breaking perturbation. To show this, we consider

$$\hat{H}^{\rm sb}_{\rm eff}(\mathbf{k}) = \delta(k_x + \sqrt{3}k_y)\tau_z \otimes \sigma_z, \tag{3.6}$$

which respects reflection and time-reversal symmetry. In the presence of this term Hamiltonian (3.3) exhibits two Weyl rings within the mirror plane $k_z = 0$ with in-plane momenta given by the equation $(k_x \pm \delta/2)^2 + (k_y \pm \sqrt{3}\delta/2)^2 = k_0^2 + \delta^2$. These two Weyl rings intersect on the $(\sqrt{3}, -1, 0)$ axis, where the gap term (3.6) vanishes [cf. Fig. 6(c)]. We find again that these Weyl rings are protected by the mirror number (2.7), with

$$n^{+,0}_{\rm occ}(k_\parallel) = \begin{cases} 1, & \left(k_x \pm \frac{\delta}{2}\right)^2 + \left(k_y \pm \frac{\sqrt{3}\delta}{2}\right)^2 > k_0^2 + \delta^2 \quad \text{and} \\ & \left(k_x \mp \frac{\delta}{2}\right)^2 + \left(k_y \mp \frac{\sqrt{3}\delta}{2}\right)^2 < k_0^2 + \delta^2, \\ 0, & \text{otherwise.} \end{cases} \tag{3.7}$$

Figure 6(d) shows the surface spectrum of $\hat{H}_{\rm eff}$ perturbed by Eq. (3.6). As for the tight-binding model with the inversion-breaking term (2.17), there appear two drumhead surface states. We note that $PbTaSe_2$ [51,52] and $TlTaSe_2$ [53] are examples of inversion-breaking semimetals with Weyl nodal lines. The low-energy physics of these materials can be described by the effective theory (3.3) perturbed by a term of the form (3.6).

IV. SUMMARY AND DISCUSSION

In this paper we have studied the topological stability of Dirac and Weyl line nodes of three-dimensional semimetals in the presence of reflection symmetry, time-reversal symmetry, inversion symmetry, and SU(2) spin-rotation symmetry. We have shown that when spin-rotation symmetry is preserved, the Dirac line is protected by either reflection symmetry or the product of inversion with time-reversal symmetry IT. In the former case, the nodal lines are classified by an $M\mathbb{Z}$ invariant [18], which takes the form of a mirror number; see Eq. (2.7). In the latter case the stability of the Dirac line is guaranteed by a quantized nonzero Berry phase, which leads to a $\mathbb{Z}_2$ classification; see Eq. (2.9). Even though the mirror invariant (2.7) does not directly give rise to topological surface states, Dirac line semimetals generically exhibit drumhead surface states which are due to the Berry phase (2.9). By deriving a relation between the mirror number (2.7) and the Berry phase (2.9), we have established a direct connection between the existence of drumhead surface states and the topological stability of Dirac nodal lines in the bulk; see Eq. (2.11). Moreover, this relation shows that the Berry phase

can be simply obtained by computing the reflection parity eigenvalues, in a similar way to that in inversion-symmetric topological insulators [81].

As a representative example of a line node semimetal, we have considered Ca_3P_2 [55]. Among the recently discovered nodal line semimetal compounds [51–56], Ca_3P_2 is the only one whose Dirac ring is at the Fermi energy and which can be grown in single-crystal form [55]. Hence, this material is ideal for experimental studies of the drumhead surface states and the unconventional transport properties of nodal line semimetals. From *ab initio* DFT calculations we have derived a tight-binding and low-energy continuum description of Ca_3P_2. By computing the mirror number and the quantized Berry phase (Fig. 3), we have shown that the Dirac band crossing of Ca_3P_2 is protected by reflection or IT symmetry. Furthermore, we have computed the surface spectrum of Ca_3P_2 and shown that its drumhead surface state is weakly dispersing with an effective mass $m^* \simeq 4m_e$ [Figs. 3(b) and 3(d)]. The weak dispersion of the surface state gives rise to a large density of states thereby enhancing interaction effects. Therefore, even small interactions may lead to unusual symmetry-broken states at the surface of Ca_3P_2, such as surface superconductivity [46,47] or surface magnetism [48]. Our low-energy descriptions, Eqs. (2.2) and (3.1), will serve as an important basis for future studies of the unconventional properties of nodal line systems, for example their unconventional transport phenomena. We note that the continuum Hamiltonian (3.1) captures the low-energy physics of any Dirac (or Weyl) nodal line semimetal, while the tight-binding Hamiltonian (2.2) describes, besides Ca_3P_2, also the nodal line of the structurally identical semimetal Zr_5Si_3.

In Ca_3P_2 spin-rotation symmetry is conserved to a very good approximation, since spin-orbit coupling for the light elements Ca and P is very small. However, there are nodal line semimetals with heavy atoms, such as $PbTaSe_2$ and $TlTaSe_2$, in which spin-rotation symmetry is broken, due to the non-negligible spin-orbit interactions. In these systems the fourfold degenerate Dirac rings are unstable. Twofold degenerate Weyl rings, on the other hand, can be protected against gap opening by reflection symmetry, provided either time-reversal or reflection symmetry is broken. We have shown that the stability of these Weyl rings is guaranteed by the mirror invariant (2.7). Similarly to the Dirac nodal line semimetals, Weyl ring semimetals support drumhead surface states (Figs. 5 and 6). The region in the surface Brillouin zone where these drumhead states appear is bounded by the projected Weyl rings.

Determining the stability of the drumhead surface states against disorder, which breaks the crystalline symmetries that protect the surface states, needs a careful analysis of different types of scattering processes, involving both states near the bulk line nodes and surface states. For the case of crystalline topological insulators it has been shown that the surface states are robust against disorder when the disorder respects the crystal symmetries on average [82]. In Appendix D, we study this question in terms of a one-dimensional reflection-symmetric toy model with a quantized Berry phase. In order to infer how impurity scattering affects the topological properties, we determine the charge that is accumulated at the two ends of this one-dimensional system [80]. We find that even in the presence of disorder that respects reflection symmetry on average, the end charges remain to a good approximation quantized to $\pm e/2$. Due to Eq. (2.10), which relates the end charges to the Berry phase, this indicates that the bulk topological properties remain unaffected by this type of disorder. This finding suggest that the drumhead surface states of nodal line semimetals are not destroyed by impurities, as long as the disorder respects reflection symmetry on average and its strength is smaller than the energy gap between the conduction and valence bands.

In conclusion, Dirac ring and Weyl ring semimetals are a new type of topological material which is characterized by a nonzero mirror invariant and a quantized Berry phase. The nontrivial band topology of these systems manifests itself at the surface in terms of a protected drumhead surface state. The dispersion minimum of this drumhead state gives rise to a Van Hove singularity in the surface density of states, which can serve as an experimental fingerprint of topological nodal line semimetals. There are many interesting avenues for future research on line node semimetals. For example, the drumhead states may give rise to unusual correlation physics at the surface. Another promising direction for future work is the study of novel topological response phenomena in these systems.

Note added. Recently we became aware of a study by Yamakage *et al.* [83], which discusses the topology of line node semimetals in terms of a k-independent reflection operator, using a k-dependent gauge transformation.

ACKNOWLEDGMENTS

The authors thank M. Franz, G. Bian, T. Heikkilä, T. Hyart, L. Schoop, and D.-H. Xu for useful discussions. The support of the Max-Planck-UBC Centre for Quantum Materials is gratefully acknowledged. A.P.S. was supported in part by the National Science Foundation under Grant No.NSF PHY11-25915. C.C.K. was also supported by Microsoft and LPS-MPO-CMTC during the last stage of this work. Y.H.C. is supported by a Thematic Project at Academia Sinica. M.Y.C. acknowledges support by the US Department of Energy, Office of Science, Office of Basic Energy Sciences, under Award No. DE-FG02-97ER45632.

APPENDIX A: DETAILS OF THE TIGHT-BINDING MODEL

In this Appendix we give a detailed description of the tight-binding Hamiltonian of Sec. II.

1. Matrix elements

The matrix elements given below closely follow Eq. (2.2). The position vectors $\mathbf{s}_\alpha$ of each orbital are listed in Table I. We illustrate each hopping terms in Fig. 7.

a. Ca-Ca matrix elements

In the H_{Ca} block, we can further divide orbitals in each atomic species into those belonging to the lower layer and the upper layer,

$$H_{\mathrm{Ca}} = \begin{pmatrix} H_{\mathrm{Ca}}^{ll} & H_{\mathrm{Ca}}^{lu} \\ H_{\mathrm{Ca}}^{lu\,\dagger} & H_{\mathrm{Ca}}^{uu} \end{pmatrix}, \tag{A1}$$

where subblocks $H_{\mathrm{Ca}}^{ll}, H_{\mathrm{Ca}}^{uu}$, and H_{Ca}^{lu} are 3×3 matrices.

TABLE I. Position vectors $\mathbf{s}_\alpha$ of each orbital. All vectors are given in the crystal coordinate system, which is indicated by the red/green arrows in Fig. 7. The lattice vectors are $\mathbf{a} = [7.150, -4.218, 0.000]$, $\mathbf{b} = [0.000, 8.256, 0.000]$, and $\mathbf{c} = [0.000, 0.000, 6.836]$ in units of Å.

α	Orbital	$\mathbf{s}_\alpha$
1	Ca1	(0.2029, 0.0, 0.25)
2	Ca2	(−0.2029, −0.2029, 0.25)
3	Ca3	(0.0, 0.2029, 0.25)
4	Ca4	(−0.2029, 0.0, −0.25)
5	Ca5	(0.2029, 0.2029, −0.25)
6	Ca6	(0.0, −0.2029, −0.25)
7	P1	(0.6215, 0.0, 0.25)
8	P2	(−0.6215, −0.6215, 0.25)
9	P3	(0.0, 0.6215, 0.25)
10	P4	(−0.6215, 0.0, −0.25)
11	P5	(0.6215, 0.6215, −0.25)
12	P6	(0.0, −0.6215, −0.25)

The Hamiltonian matrices H_{Ca}^{ll} and H_{Ca}^{uu} have 3 independent intralayer hopping terms, the nearest-neighbor, second-nearest-neighbor, and third-nearest-neighbor hoppings, td_2, td_4, and td_5, as shown in Fig. 7:

$$H_{\mathrm{Ca}}^{ll} = \begin{pmatrix} h_{11}^{c,ll} & h_{12}^{c,ll} & h_{13}^{c,ll} \\ h_{21}^{c,ll} & h_{22}^{c,ll} & h_{23}^{c,ll} \\ h_{31}^{c,ll} & h_{32}^{c,ll} & h_{33}^{c,ll} \end{pmatrix}, \tag{A2}$$

where

$$h_{12}^{c,ll} = e^{i\mathbf{k}\cdot\mathbf{s}_{1,2}}\left(td_2 + td_4 c_{12}^4 + td_5 c_{12}^5\right), \tag{A3}$$

$$h_{13}^{c,ll} = e^{i\mathbf{k}\cdot\mathbf{s}_{1,3}}\left(td_2 + td_4 c_{13}^4 + td_5 c_{13}^5\right), \tag{A4}$$

$$h_{23}^{c,ll} = e^{i\mathbf{k}\cdot\mathbf{s}_{2,3}}\left(td_2 + td_4 c_{23}^4 + td_5 c_{23}^5\right), \tag{A5}$$

and $h_{11}^{c,ll} = h_{22}^{c,ll} = h_{33}^{c,ll} = \mu_d$. We define phase factors $c_{\alpha\beta}^i$ for hopping integral td_i with matrix indices α and β:

$$c_{12}^4 = e^{i\mathbf{k}\cdot\mathbf{R}_{100}} + e^{i\mathbf{k}\cdot\mathbf{R}_{110}}, \tag{A6}$$

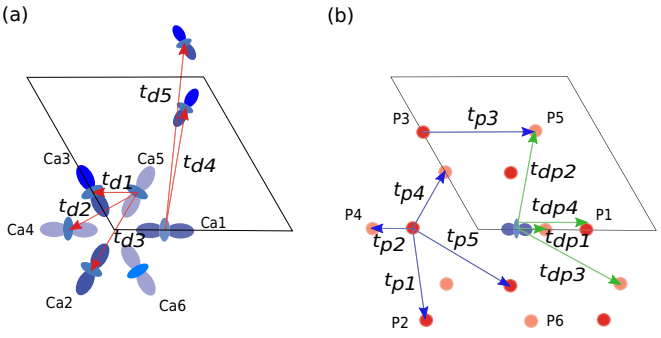

FIG. 7. (a) Definitions of hopping integrals between two Ca orbitals. (b) Definitions of hopping integrals between two P orbitals and one Ca and one P orbital. Orbitals in the first Brillouin zone are labeled. Dark blue and red color represent orbitals in the lower plane while light blue and pink orbitals lie in the upper plane.

$$c_{13}^4 = e^{i\mathbf{k}\cdot\mathbf{R}_{100}} + e^{i\mathbf{k}\cdot\mathbf{R}_{0-10}}, \tag{A7}$$

$$c_{23}^4 = e^{i\mathbf{k}\cdot\mathbf{R}_{-1-10}} + e^{i\mathbf{k}\cdot\mathbf{R}_{0-10}}, \tag{A8}$$

$$c_{12}^5 = e^{i\mathbf{k}\cdot\mathbf{R}_{010}} + e^{i\mathbf{k}\cdot\mathbf{R}_{0-10}}, \tag{A9}$$

$$c_{13}^5 = e^{i\mathbf{k}\cdot\mathbf{R}_{110}} + e^{i\mathbf{k}\cdot\mathbf{R}_{-1-10}}, \tag{A10}$$

$$c_{23}^5 = e^{i\mathbf{k}\cdot\mathbf{R}_{-100}} + e^{i\mathbf{k}\cdot\mathbf{R}_{100}}, \tag{A11}$$

where $\mathbf{R}_{ijk}$ is the lattice vector connecting the unit cell in the (i,j,k) direction and $\mathbf{s}_{l,m} = \mathbf{s}_m - \mathbf{s}_l$. H_{Ca}^{uu} is defined similarly.

H_{Ca}^{lu} contains 2 independent interplane hopping integrals td_1 and td_3:

$$H_{\mathrm{Ca}}^{lu} = c_0 \begin{pmatrix} td_3 e^{i\mathbf{k}\cdot\mathbf{s}_{1,4}} & td_1 e^{i\mathbf{k}\cdot\mathbf{s}_{1,5}} & td_1 e^{i\mathbf{k}\cdot\mathbf{s}_{1,6}} \\ td_1 e^{i\mathbf{k}\cdot\mathbf{s}_{2,4}} & td_3 e^{i\mathbf{k}\cdot\mathbf{s}_{2,5}} & td_1 e^{i\mathbf{k}\cdot\mathbf{s}_{2,6}} \\ td_1 e^{i\mathbf{k}\cdot\mathbf{s}_{3,4}} & td_1 e^{i\mathbf{k}\cdot\mathbf{s}_{3,5}} & td_3 e^{i\mathbf{k}\cdot\mathbf{s}_{3,6}} \end{pmatrix}, \tag{A12}$$

where c_0 is $(1 + e^{i\mathbf{k}\cdot\mathbf{R}_{001}})$.

b. P-P matrix elements

We apply similar division of layer indices for H_{P} matrix:

$$H_{\mathrm{P}} = \begin{pmatrix} H_{\mathrm{P}}^{ll} & H_{\mathrm{P}}^{lu} \\ H_{\mathrm{P}}^{lu\dagger} & H_{\mathrm{P}}^{uu} \end{pmatrix}. \tag{A13}$$

The Hamiltonian matrices H_{P}^{ll} and H_{P}^{uu} have 2 independent hopping integrals tp_1 and tp_5 coupling orbitals in the same layer:

$$H_{\mathrm{P}}^{ll} = \begin{pmatrix} h_{11}^{p,ll} & h_{12}^{p,ll} & h_{13}^{p,ll} \\ h_{21}^{p,ll} & h_{22}^{p,ll} & h_{23}^{p,ll} \\ h_{31}^{p,ll} & h_{32}^{p,ll} & h_{33}^{p,ll} \end{pmatrix}, \tag{A14}$$

where

$$h_{12}^{p,ll} = e^{i\mathbf{k}\cdot\mathbf{s}_{7,8}}\left(tp_5 + tp_1 a_{12}^1\right), \tag{A15}$$

$$h_{13}^{p,ll} = e^{i\mathbf{k}\cdot\mathbf{s}_{7,9}}\left(tp_5 + tp_1 a_{13}^1\right), \tag{A16}$$

$$h_{23}^{p,ll} = e^{i\mathbf{k}\cdot\mathbf{s}_{8,9}}\left(tp_5 + tp_1 a_{23}^1\right), \tag{A17}$$

and $h_{11}^{p,ll} = h_{22}^{p,ll} = h_{33}^{p,ll} = \mu_p$. $a_{\alpha\beta}^i$ are phase factors from hopping tp_i with matrix index α and β,

$$a_{12}^1 = e^{i\mathbf{k}\cdot\mathbf{R}_{100}} + e^{i\mathbf{k}\cdot\mathbf{R}_{110}}, \tag{A18}$$

$$a_{13}^1 = e^{i\mathbf{k}\cdot\mathbf{R}_{100}} + e^{i\mathbf{k}\cdot\mathbf{R}_{0-10}}, \tag{A19}$$

$$a_{23}^1 = e^{i\mathbf{k}\cdot\mathbf{R}_{-1-10}} + e^{i\mathbf{k}\cdot\mathbf{R}_{0-10}}. \tag{A20}$$

H_{P}^{uu} can be defined similarly.

H_{P}^{lu} contains 3 independent interplane hopping integrals tp_2,tp_3, and tp_4:

$$H_{\mathrm{P}}^{lu} = \begin{pmatrix} h_{11}^{p,lu} & h_{12}^{p,lu} & h_{13}^{p,lu} \\ h_{21}^{p,lu} & h_{22}^{p,lu} & h_{23}^{p,lu} \\ h_{31}^{p,lu} & h_{32}^{p,lu} & h_{33}^{p,lu} \end{pmatrix}, \tag{A21}$$

where

$$h_{11}^{p,lu} = tp_2 e^{i\mathbf{k}\cdot\mathbf{s}_{7,10}}(e^{i\mathbf{k}\cdot\mathbf{R}_{100}} + e^{i\mathbf{k}\cdot\mathbf{R}_{101}}), \quad \text{(A22)}$$

$$h_{22}^{p,lu} = tp_2 e^{i\mathbf{k}\cdot\mathbf{s}_{8,11}}(e^{i\mathbf{k}\cdot\mathbf{R}_{-1-10}} + e^{i\mathbf{k}\cdot\mathbf{R}_{-1-11}}), \quad \text{(A23)}$$

$$h_{33}^{p,lu} = tp_2 e^{i\mathbf{k}\cdot\mathbf{s}_{9,12}}(e^{i\mathbf{k}\cdot\mathbf{R}_{010}} + e^{i\mathbf{k}\cdot\mathbf{R}_{011}}), \quad \text{(A24)}$$

and

$$h_{12}^{p,lu} = e^{i\mathbf{k}\cdot\mathbf{s}_{7,11}}\left(tp_3 c_0 + tp_4 a_{12}^4\right), \quad \text{(A25)}$$

$$h_{13}^{p,lu} = e^{i\mathbf{k}\cdot\mathbf{s}_{7,12}}\left(tp_3 c_0 + tp_4 a_{13}^4\right), \quad \text{(A26)}$$

$$h_{21}^{p,lu} = e^{i\mathbf{k}\cdot\mathbf{s}_{8,10}}\left(tp_3 c_0 + tp_4 a_{21}^4\right), \quad \text{(A27)}$$

$$h_{23}^{p,lu} = e^{i\mathbf{k}\cdot\mathbf{s}_{8,12}}\left(tp_3 c_0 + tp_4 a_{23}^4\right), \quad \text{(A28)}$$

$$h_{31}^{p,lu} = e^{i\mathbf{k}\cdot\mathbf{s}_{9,10}}\left(tp_3 c_0 + tp_4 a_{31}^4\right), \quad \text{(A29)}$$

$$h_{32}^{p,lu} = e^{i\mathbf{k}\cdot\mathbf{s}_{9,11}}\left(tp_3 c_0 + tp_4 a_{32}^4\right). \quad \text{(A30)}$$

The corresponding phase factors are

$$c_0 = 1 + e^{i\mathbf{k}\cdot\mathbf{R}_{001}}, \quad \text{(A31)}$$

$$a_{12}^4 = e^{i\mathbf{k}\cdot\mathbf{R}_{0-10}} + e^{i\mathbf{k}\cdot\mathbf{R}_{0-11}}, \quad \text{(A32)}$$

$$a_{13}^4 = e^{i\mathbf{k}\cdot\mathbf{R}_{110}} + e^{i\mathbf{k}\cdot\mathbf{R}_{111}}, \quad \text{(A33)}$$

$$a_{21}^4 = e^{i\mathbf{k}\cdot\mathbf{R}_{0-10}} + e^{i\mathbf{k}\cdot\mathbf{R}_{0-11}}, \quad \text{(A34)}$$

$$a_{23}^4 = e^{i\mathbf{k}\cdot\mathbf{R}_{-100}} + e^{i\mathbf{k}\cdot\mathbf{R}_{-101}}, \quad \text{(A35)}$$

$$a_{31}^4 = e^{i\mathbf{k}\cdot\mathbf{R}_{110}} + e^{i\mathbf{k}\cdot\mathbf{R}_{111}}, \quad \text{(A36)}$$

$$a_{32}^4 = e^{i\mathbf{k}\cdot\mathbf{R}_{-100}} + e^{i\mathbf{k}\cdot\mathbf{R}_{-101}}. \quad \text{(A37)}$$

c. Ca-P matrix elements

Finally, the interorbital hopping matrix V describes the hybridization between Ca and P orbitals. We again divide V into four 3×3 matrices according to their layer indices,

$$V = \begin{pmatrix} V^{ll} & V^{lu} \\ V^{ul} & V^{uu} \end{pmatrix}. \quad \text{(A38)}$$

The V^{ll} and V^{uu} blocks only have diagonal elements, which can be written down with the hopping integrals tdp_4,

$$V^{ll} = b_1\, tdp_4 \begin{pmatrix} e^{i\mathbf{k}\cdot\mathbf{s}_{1,7}} & 0 & 0 \\ 0 & e^{i\mathbf{k}\cdot\mathbf{s}_{2,8}} & 0 \\ 0 & 0 & e^{i\mathbf{k}\cdot\mathbf{s}_{3,9}} \end{pmatrix} \quad \text{(A39)}$$

and

$$V^{uu} = -b_1\, tdp_4 \begin{pmatrix} e^{i\mathbf{k}\cdot\mathbf{s}_{4,10}} & 0 & 0 \\ 0 & e^{i\mathbf{k}\cdot\mathbf{s}_{5,11}} & 0 \\ 0 & 0 & e^{i\mathbf{k}\cdot\mathbf{s}_{6,12}} \end{pmatrix}, \quad \text{(A40)}$$

where the phase factor $b_1 = (e^{i\mathbf{k}\cdot\mathbf{R}_{001}} - e^{i\mathbf{k}\cdot\mathbf{R}_{00-1}})$. We note that the minus sign in V^{uu} is due to the opposite orientation of p_x orbitals in the different layer. Also due to the opposite inversion symmetry eigenvalue of the p_x and the d_{z^2} orbital, hopping integrals vanish if both of them lie in the same plane. Hence, only hopping integrals from different unit cells contribute to diagonal elements.

Interlayer coupling $tdp1$,$tdp2$, and $tdp3$ contributes to V^{lu} and V^{ul} matrices,

$$V^{lu} = \begin{pmatrix} V_{11}^{lu} & V_{12}^{lu} & V_{13}^{lu} \\ V_{21}^{lu} & V_{22}^{lu} & V_{23}^{lu} \\ V_{31}^{lu} & V_{32}^{lu} & V_{33}^{lu} \end{pmatrix}, \quad \text{(A41)}$$

where

$$V_{11}^{lu} = -tdp_1 e^{i\mathbf{k}\cdot\mathbf{s}_{1,10}}(e^{i\mathbf{k}\cdot\mathbf{R}_{101}} - e^{i\mathbf{k}\cdot\mathbf{R}_{100}}), \quad \text{(A42)}$$

$$V_{22}^{lu} = -tdp_1 e^{i\mathbf{k}\cdot\mathbf{s}_{2,11}}(e^{i\mathbf{k}\cdot\mathbf{R}_{-1-11}} - e^{i\mathbf{k}\cdot\mathbf{R}_{-1-10}}), \quad \text{(A43)}$$

$$V_{33}^{lu} = -tdp_1 e^{i\mathbf{k}\cdot\mathbf{s}_{3,12}}(e^{i\mathbf{k}\cdot\mathbf{R}_{011}} - e^{i\mathbf{k}\cdot\mathbf{R}_{010}}), \quad \text{(A44)}$$

and off-diagonal elements

$$V_{12}^{lu} = e^{i\mathbf{k}\cdot\mathbf{s}_{1,11}}\left(tdp_2 b_2 + tdp_3 b_{12}^3\right), \quad \text{(A45)}$$

$$V_{13}^{lu} = e^{i\mathbf{k}\cdot\mathbf{s}_{1,12}}\left(tdp_2 b_2 + tdp_3 b_{13}^3\right), \quad \text{(A46)}$$

$$V_{21}^{lu} = e^{i\mathbf{k}\cdot\mathbf{s}_{2,10}}\left(tdp_2 b_2 + tdp_3 b_{21}^3\right), \quad \text{(A47)}$$

$$V_{23}^{lu} = e^{i\mathbf{k}\cdot\mathbf{s}_{2,12}}\left(tdp_2 b_2 + tdp_3 b_{23}^3\right), \quad \text{(A48)}$$

$$V_{31}^{lu} = e^{i\mathbf{k}\cdot\mathbf{s}_{3,10}}\left(tdp_2 b_2 + tdp_3 b_{31}^3\right), \quad \text{(A49)}$$

$$V_{32}^{lu} = e^{i\mathbf{k}\cdot\mathbf{s}_{3,11}}\left(tdp_2 b_2 + tdp_3 b_{32}^3\right). \quad \text{(A50)}$$

The phase factors are

$$b_2 = -(e^{i\mathbf{k}\cdot\mathbf{R}_{001}} - e^{i\mathbf{k}\cdot\mathbf{R}_{000}}), \quad \text{(A51)}$$

$$b_{12}^3 = -(e^{i\mathbf{k}\cdot\mathbf{R}_{0-11}} - e^{i\mathbf{k}\cdot\mathbf{R}_{0-10}}), \quad \text{(A52)}$$

$$b_{13}^3 = -(e^{i\mathbf{k}\cdot\mathbf{R}_{111}} - e^{i\mathbf{k}\cdot\mathbf{R}_{110}}), \quad \text{(A53)}$$

$$b_{21}^3 = -(e^{i\mathbf{k}\cdot\mathbf{R}_{0-11}} - e^{i\mathbf{k}\cdot\mathbf{R}_{0-10}}), \quad \text{(A54)}$$

$$b_{23}^3 = -(e^{i\mathbf{k}\cdot\mathbf{R}_{-101}} - e^{i\mathbf{k}\cdot\mathbf{R}_{-100}}), \quad \text{(A55)}$$

$$b_{31}^3 = -(e^{i\mathbf{k}\cdot\mathbf{R}_{111}} - e^{i\mathbf{k}\cdot\mathbf{R}_{110}}), \quad \text{(A56)}$$

$$b_{32}^3 = -(e^{i\mathbf{k}\cdot\mathbf{R}_{-101}} - e^{i\mathbf{k}\cdot\mathbf{R}_{-100}}), \quad \text{(A57)}$$

where $b_{\alpha\beta}^i$ belongs to hopping tdp_i between index α and β.

Similarly, we have

$$V^{ul} = \begin{pmatrix} V_{11}^{ul} & V_{12}^{ul} & V_{13}^{ul} \\ V_{21}^{ul} & V_{22}^{ul} & V_{23}^{ul} \\ V_{31}^{ul} & V_{32}^{ul} & V_{33}^{ul} \end{pmatrix}, \quad \text{(A58)}$$

where

$$V_{11}^{ul} = -tdp_1 e^{i\mathbf{k}\cdot\mathbf{s}_{4,7}}(e^{i\mathbf{k}\cdot\mathbf{R}_{-10-1}} - e^{i\mathbf{k}\cdot\mathbf{R}_{-100}}), \quad \text{(A59)}$$

$$V_{22}^{ul} = -tdp_1 e^{i\mathbf{k}\cdot\mathbf{s}_{5,8}}(e^{i\mathbf{k}\cdot\mathbf{R}_{11-1}} - e^{i\mathbf{k}\cdot\mathbf{R}_{1110}}), \quad \text{(A60)}$$

$$V_{33}^{ul} = -tdp_1 e^{i\mathbf{k}\cdot\mathbf{s}_{6,9}}(e^{i\mathbf{k}\cdot\mathbf{R}_{0-1-1}} - e^{i\mathbf{k}\cdot\mathbf{R}_{0-10}}), \quad \text{(A61)}$$

and off-diagonal elements

$$V_{12}^{ul} = e^{i\mathbf{k}\cdot\mathbf{s}_{4,8}}\left(tdp_2 b_2 + tdp_3 b_{12}^3\right)^*, \quad \text{(A62)}$$

$$V_{13}^{ul} = e^{i\mathbf{k}\cdot\mathbf{s}_{4,9}}\left(tdp_2 b_2 + tdp_3 b_{13}^3\right)^*, \quad \text{(A63)}$$

$$V_{21}^{ul} = e^{i\mathbf{k}\cdot\mathbf{s}_{5,7}}\left(tdp_2 b_2 + tdp_3 b_{21}^3\right)^*, \quad \text{(A64)}$$

$$V_{23}^{ul} = e^{i\mathbf{k}\cdot\mathbf{s}_{5,9}}\left(tdp_2 b_2 + tdp_3 b_{23}^3\right)^*, \quad \text{(A65)}$$

$$V_{31}^{ul} = e^{i\mathbf{k}\cdot\mathbf{s}_{6,7}}\left(tdp_2 b_2 + tdp_3 b_{31}^3\right)^*, \quad \text{(A66)}$$

$$V_{32}^{ul} = e^{i\mathbf{k}\cdot\mathbf{s}_{6,8}}\left(tdp_2 b_2 + tdp_3 b_{32}^3\right)^*, \quad \text{(A67)}$$

where * denotes the complex conjugate.

2. Tight-binding parameters

We list the parameters of the tight-binding model in units of eV below. The hopping integrals between two Ca orbitals are $td_1 = -0.2031$, $td_2 = -0.6388$, $td_3 = -0.0786$, $td_4 = -0.216$, and $td_5 = 0.0516$. Those between two P orbitals are $tp_1 = -0.041$, $tp_2 = -0.4077$, $tp_3 = -0.0479$, $tp_4 = -0.1067$, and $tp_5 = 0.0548$. Finally, the hopping amplitudes between Ca and P orbitals are $tdp_1 = 0.1415$, $tdp_2 = 0.0379$, $tdp_3 = 0.0443$ and $tdp_4 = 0.0376$. The chemical potentials are $\mu_d = 2.6808$ and $\mu_p = -1.2186$ for Ca and P, respectively.

APPENDIX B: TOPOLOGICAL NUMBER AND BERRY PHASE

To show that the Berry phase in the k_z direction is quantized and is related to $n_{\rm occ}^+$ in Eq. (2.11), we recall some basic facts of inversion symmetry. We assume no degeneracies so the inversion symmetry acts on the wave functions $|u_{k,j}\rangle$ in the unique expression ($k \equiv k_z$)

$$|u_{-k,j}\rangle = e^{-i\alpha_k^j} R_k |u_{k,j}\rangle. \quad \text{(B1)}$$

The reflection operator obeys $R_{-k}R_k = \pm\mathbb{1}$ for spinless/spin-1/2 systems, respectively. For spin-1/2, we redefine $R_k \to -iR_k$ so that $R_{-k}R_k = \mathbb{1}$. Also, $R_k^\dagger R_k = \mathbb{1}$. Let us rewrite the Berry phase

$$\begin{aligned}\mathcal{P} &= -i\left(\int_0^\pi + \int_{-\pi}^0\right)\sum_{E_j<E_{\rm F}}\langle u_{k,j}|\partial_k|u_{k,j}\rangle dk \\ &= -i\int_0^\pi \sum_{E_j<E_{\rm F}}\langle u_{k,j}|\partial_k|u_{k,j}\rangle dk \\ &\quad + i\int_0^\pi \sum_{E_j<E_{\rm F}}\langle u_{k,j}|R_k^\dagger e^{i\alpha_k^j}\partial_k e^{-i\alpha_k^j} R_k|u_{k,j}\rangle dk \\ &= \sum_{E_j<E_{\rm F}}\left(\alpha_\pi^j - \alpha_0^j\right) + i\int_0^\pi \sum_{E_j<E_{\rm F}}\langle u_{k,j}|R_k^\dagger\partial_k R_k|u_{k,j}\rangle dk.\end{aligned} \quad \text{(B2)}$$

The reflection symmetry operator has a generic block-diagonalized from [3]

$$R_k = U_{i_1 j_1} e^{in_1 k} \oplus U_{i_2 j_2} e^{in_2 k} \oplus \ldots \oplus U_{i_N j_N} e^{in_N k}, \quad \text{(B3)}$$

where $U_{i_l j_l}$ is a unitary matrix and we use the lattice constant $a \equiv 1$:

$$R_k^\dagger \partial_k R_k = in_1\delta_{i_1 j_1} \oplus in_2\delta_{i_2 j_2} \oplus \ldots \oplus in_N\delta_{i_N j_N}. \quad \text{(B4)}$$

Hence, ∂R is just $m\pi$, where m is an integer

$$i\int_0^\pi \sum_{E_j<E_{\rm F}}\langle u_{k,j}|R_k^\dagger\partial_k R_k|u_{k,j}\rangle dk = -\sum_{l=1} n_l m_l \pi, \quad \text{(B5)}$$

where m_l is the number of the occupied states in the $U_{i_l j_l}$ block. Consider the left-hand side of Eq. (2.11),

$$\begin{aligned}n_{\rm occ}^{+,\pi} - n_{\rm occ}^{+,0} &= \frac{1}{2}\sum_{E_j<0}\left(\langle u_{\pi,j}|R_\pi|u_{\pi,j}\rangle - \langle u_{0,j}|R_0|u_{0,j}\rangle\right) \\ &= \frac{1}{2}\sum_{E_j<0}(e^{i\alpha_\pi^j} - e^{i\alpha_0^j}).\end{aligned} \quad \text{(B6)}$$

Since $R_{k_0}^\dagger = R_{k_0}$, where $k_0 = -k_0$, such as 0, π so $e^{i\alpha_{k_0}^j} = \pm 1$ and then

$$n_{\rm occ}^{+,\pi} - n_{\rm occ}^{+,0} \equiv \frac{1}{\pi}\sum_{E_j<E_{\rm F}}\left(\alpha_\pi^j - \alpha_0^j\right) \pmod 2. \quad \text{(B7)}$$

Thus, $(-1)^{n_{\rm occ}^{+,\pi} - n_{\rm occ}^{+,0}} = e^{i\sum_{E_j<E_{\rm F}}(\alpha_\pi^j - \alpha_0^j)}$. By using Eq. (B2), (B7), we obtain the relation in Eq. (2.11) between the topological invariants and the Berry phase $\mathcal{P}$ is either 0 or π (mod 2π) since the $2n\pi$ phase can be canceled by a large $U(1)$ gauge transformation.

Similarly, IT symmetry, the composite symmetry of time-reversal and inversion, also quantizes the Berry phase when $d\mathbf{k}$ is integrated along any closed loop. Since time-reversal and inversion operators both flip $\mathbf{k}$, the composite symmetry operators keep the same $\mathbf{k}$. The integration path can be arbitrarily chose to preserve IT symmetry. Unlike the Berry phase under reflection symmetry, the integration path should be strictly in the k_z direction to preserve reflection symmetry.

The IT symmetry operator is the combination of a unitary matrix and complex conjugation $T\mathcal{I} = UK$; the unitary matrix U might be $\mathbf{k}$-dependent. To simplify the problem, we assume U is $\mathbf{k}$-independent, which is the case of Ca_3P_2 tight-binding model. The relation of wave functions under IT symmetry is given by

$$|u_{\mathbf{k},j}\rangle = e^{i\beta_{\mathbf{k}}^j} U|u_{\mathbf{k},l_j}\rangle. \quad \text{(B8)}$$

We note that $|u_{\mathbf{k},j}\rangle$ and $|u_{\mathbf{k},l_j}\rangle$ in the same energy level might be orthogonal or identical. Let us show that the Berry phase is

quantized

$$\mathcal{P} = -i \oint \sum_{E_j<E_F} \langle u_{\mathbf{k},j}|\partial_{\mathbf{k}}|u_{\mathbf{k},j}\rangle d\mathbf{k}$$
$$= -i \oint \sum_{E_j<E_F} \langle u^*_{\mathbf{k},l_j}|U^\dagger e^{-i\beta^j_{\mathbf{k}}}\partial_{\mathbf{k}} e^{i\beta^j_{\mathbf{k}}} U|u^*_{\mathbf{k},l_j}\rangle d\mathbf{k}$$
$$= \sum_{E_j<E_F} (\beta^j_+ - \beta^j_-) - i \oint \sum_{E_j<E_F} \langle u^*_{\mathbf{k},l_j}|\partial_{\mathbf{k}}|u^*_{\mathbf{k},l_j}\rangle d\mathbf{k}, \quad \text{(B9)}$$

where $\beta^j_\mp$ represent the phases at the beginning and end of the integration path, respectively. The first summation is $2n\pi$. Since the jth and the l_jth states share the same energy and each state in the second summation should be orthogonal, we safely change the index l_j to j in the summation. We use the identity

$$\langle u^*_{\mathbf{k},j}|\partial_{\mathbf{k}}|u^*_{\mathbf{k},j}\rangle = \langle \partial_{\mathbf{k}} u_{\mathbf{k},j}|u_{\mathbf{k},j}\rangle = -\langle u_{\mathbf{k},j}|\partial_{\mathbf{k}}|u_{\mathbf{k},j}\rangle. \quad \text{(B10)}$$

It follows that the Berry phase is quantized

$$\mathcal{P} = \sum_{E_j<E_F} (\beta^j_+ - \beta^j_-) = n\pi. \quad \text{(B11)}$$

APPENDIX C: TOY MODEL OF TOPOLOGICAL NODAL LINES

The tight-binding model of Ca_3P_2 provides the way to investigate topological nodal lines in a realistic model. However, to capture the physical features of the nodal lines only the low-energy theory is needed. We extend the low-energy theory to a simple lattice model in order to provide an economic way to investigate topological nodal lines. Although the space group of Ca_3P_2 is $P6_3/mcm$, we consider a square lattice and extend and transfer the low-energy equation (3.1) with spins to the lattice form

$$H^{\text{lattice}}_{\text{spinful}}(\mathbf{k}) = \frac{v'_\parallel}{a^2} g(k_\parallel)\tau_z\sigma_0 + \frac{v_z}{c}\sin ck_z\tau_y\sigma_0 + \left[\frac{v'_0}{a^2} g(k_\parallel) + V_0\right]\tau_0\sigma_0 + H_{\cos k_z}, \quad \text{(C1)}$$

where $g(k_\parallel) = 1 + \cos ak_0 - \cos ak_x - \cos ak_y$, the lattice constants $a = 8.26$ Å and $c = 6.84$ Å, $v'_\parallel = \frac{2v_\parallel ak_0}{\sin ak_0}$, and $v'_0 = \frac{2v_0 ak_0}{\sin ak_0}$. Furthermore, we define

$$H_{\cos k_z} = (1 - \cos ck_z)(Z_\tau\tau_z\sigma_0 + Z_0\tau_0\sigma_0) \quad \text{(C2)}$$

in the simplest form so that the Berry phase inside the nodal ring is nonzero when the spin degree of freedom is neglected. By fitting the energy spectrum from the DFT calculation as $k_z = 0, \pi$, we have $Z_\tau = 0.287$ eV and $Z_0 = -0.156$ eV.

APPENDIX D: QUANTIZED END CHARGE IN THE PRESENCE OF DISORDER

To understand the robustness of the topology under disorder we consider the toy model of a 1d inversion-symmetric topological insulator. We note that in a 1d system inversion symmetry is equivalent to reflection symmetry; reflection-symmetric nodal lines with fixed k_x,k_y are equivalent to the 1d inversion-symmetric topological insulator; the Berry phase, which is the integration along the 1d Brillouin zone, is quantized. The toy model in momentum space can be simply written as

$$H(p) = (\mu + \cos p)\sigma_x + \sin p\sigma_y + \delta\cos p\mathbf{1}, \quad \text{(D1)}$$

which preserves inversion symmetry by satisfying Eq. (2.6) with inversion symmetry operator $I = \sigma_x$. Broken chiral symmetry caused by $\delta\cos p\mathbf{1}$ destroys the definition of winding number so the Berry phase is the only valid topological invariant. Furthermore, by Eq. (2.4) time-reversal symmetry is preserved with time-reversal operator $T = K$. IT symmetry also guarantees the quantized Berry phase. By choosing $\mu = 0.5$ and $\delta = 0.1$, the Berry phase $\mathcal{P} = \pi$ leads to the presence of charge $\pm e/2$ at each end, which is one of the topological features of this inversion-symmetric insulator. The sign of the charge depends on the occupation of the end mode. Hence, we can numerically compute the charge on one of the ends. If the charge is no longer $\pm e/2$ in the presence of disorder, then this indicates that the nontrivial topology is destroyed by the disorder.

We add inversion symmetry breaking disorder $r_j c^\dagger_j\sigma_z c_j$ to the Hamiltonian in real space

$$\hat{H} = \sum_j \left[\frac{\mu}{2} c^\dagger_j\sigma_x c_j + c^\dagger_{j+1}\frac{\sigma_x + \delta\mathbf{1} + i\sigma_y}{2} c_j + \text{H.c.}\right], \quad \text{(D2)}$$

where r_j is a random number from $-\Delta + m$ to $\Delta + m$. When $m = 0$, the average $\langle r_j\rangle = 0$ indicates the average disorder preserves inversion symmetry. As shown in Fig. 8(a) when $m = 0$, the charge on one end is $\pm e/2$ on average. When inversion symmetry is broken on average, the charge is no longer quantized and then the topological phase is destroyed. In Fig. 8(b) the standard deviation of the disorder is proportional to the deviation of the end disorder. Thus, the quantized end charges survive when disorder on average is zero and the fluctuation is small enough.

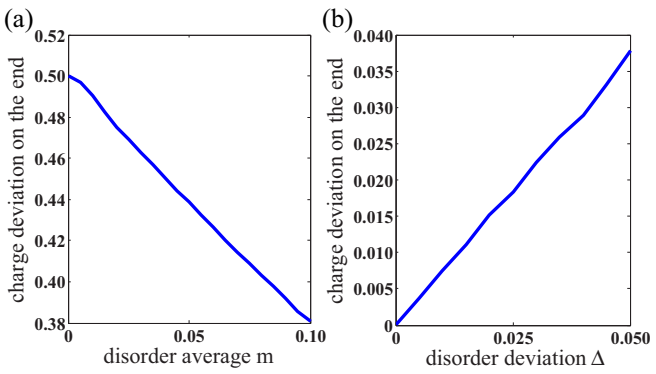

FIG. 8. The numerical result for the 1d inversion-symmetric topological insulator with 200 sites. We consider the half-filling scenario and compute the absolute value of charge accumulated on the first 10 sites under Gaussian disorder as fixed disorder average m and disorder random deviation Δ 3000 times. (a) As $\Delta = 0.02$, the end charge is not quantized when the average disorder is not zero. In the special condition that the average disorder vanishes so inversion symmetry on average is preserved, the end charge on average is $\pm e/2$. (b) The standard deviation of the disorder grows as the deviation of the end disorder grows.

[1] M. Z. Hasan and C. L. Kane, Rev. Mod. Phys. **82**, 3045 (2010).
[2] X.-L. Qi and S.-C. Zhang, Rev. Mod. Phys. **83**, 1057 (2011).
[3] C.-K. Chiu, J. C. Y. Teo, A. P. Schnyder, and S. Ryu, arXiv:1505.03535.
[4] A. P. Schnyder, S. Ryu, A. Furusaki, and A. W. W. Ludwig, Phys. Rev. B **78**, 195125 (2008).
[5] S. Ryu, A. P. Schnyder, A. Furusaki, and A. W. W. Ludwig, New J. Phys. **12**, 065010 (2010).
[6] D. Hsieh, D. Qian, L. Wray, Y. Xia, Y. S. Hor, R. J. Cava, and M. Z. Hasan, Nature (London) **452**, 970 (2008).
[7] D. Hsieh, Y. Xia, D. Qian, L. Wray, J. H. Dil, F. Meier, J. Osterwalder, L. Patthey, J. G. Checkelsky, N. P. Ong, A. V. Fedorov, H. Lin, A. Bansil, D. Grauer, Y. S. Hor, R. J. Cava, and M. Z. Hasan, Nature (London) **460**, 1101 (2009).
[8] Y. Xia, D. Qian, D. Hsieh, L. Wray, A. Pal, H. Lin, A. Bansil, D. Grauer, Y. S. Hor, R. J. Cava, and M. Z. Hasan, Nat. Phys. **5**, 398 (2009).
[9] Y. Ando, J. Phys. Soc. Jpn. **82**, 102001 (2013).
[10] M. Z. Hasan and J. E. Moore, Annu. Rev. Condens. Matter Phys. **2**, 55 (2011).
[11] M. Z. Hasan, S.-Y. Xu, and M. Neupane, *Topological Insulators, Topological Dirac Semimetals, Topological Crystalline Insulators, and Topological Kondo Insulators* (John Wiley and Sons, New York, 2015).
[12] X.-L. Qi, T. L. Hughes, and S.-C. Zhang, Phys. Rev. B **78**, 195424 (2008).
[13] X.-L. Qi, T. L. Hughes, and S.-C. Zhang, Nat. Phys. **4**, 273 (2008).
[14] I. Garate and M. Franz, Phys. Rev. B **81**, 172408 (2010).
[15] S.-Y. Xu, I. Belopolski, N. Alidoust, M. Neupane, G. Bian, C. Zhang, R. Sankar, G. Chang, Z. Yuan, C.-C. Lee, S.-M. Huang, H. Zheng, J. Ma, D. S. Sanchez, B. Wang, A. Bansil, F. Chou, P. P. Shibayev, H. Lin, S. Jia, and M. Z. Hasan, Science **349**, 613 (2015).
[16] S. Matsuura, P.-Y. Chang, A. P. Schnyder, and S. Ryu, New J. Phys. **15**, 065001 (2013).
[17] Y. X. Zhao and Z. D. Wang, Phys. Rev. Lett. **110**, 240404 (2013).
[18] C.-K. Chiu and A. P. Schnyder, Phys. Rev. B **90**, 205136 (2014).
[19] C. Fang, Y. Chen, H.-Y. Kee, and L. Fu, Phys. Rev. B **92**, 081201 (2015).
[20] A. A. Burkov, M. D. Hook, and L. Balents, Phys. Rev. B **84**, 235126 (2011).
[21] Y. X. Zhao and Z. D. Wang, Phys. Rev. B **89**, 075111 (2014).
[22] O. Vafek and A. Vishwanath, Annu. Rev. Condens. Matter Phys. **5**, 83 (2014).
[23] W. Witczak-Krempa, G. Chen, Y. B. Kim, and L. Balents, Annu. Rev. Condens. Matter Phys. **5**, 57 (2014).
[24] P. Hosur and X. Qi, C. R. Phys. **14**, 857 (2013).
[25] L. Lu, Z. Wang, D. Ye, L. Ran, L. Fu, J. D. Joannopoulos, and M. Soljačić, Science **349**, 622 (2015).
[26] B. Q. Lv, H. M. Weng, B. B. Fu, X. P. Wang, H. Miao, J. Ma, P. Richard, X. C. Huang, L. X. Zhao, G. F. Chen, Z. Fang, X. Dai, T. Qian, and H. Ding, Phys. Rev. X **5**, 031013 (2015).
[27] Z. Gao, M. Hua, H. Zhang, and X. Zhang, arXiv:1507.07504.
[28] Y. Kim, B. J. Wieder, C. L. Kane, and A. M. Rappe, Phys. Rev. Lett. **115**, 036806 (2015).
[29] H. Weng, Y. Liang, Q. Xu, R. Yu, Z. Fang, X. Dai, and Y. Kawazoe, Phys. Rev. B **92**, 045108 (2015).
[30] Y. Chen, Y. Xie, S. A. Yang, H. Pan, F. Zhang, M. L. Cohen, and S. Zhang, Nano Lett. **15**, 6974 (2015).
[31] S. Jeon, B. B. Zhou, A. Gyenis, B. E. Feldman, I. Kimchi, A. C. Potter, Q. D. Gibson, R. J. Cava, A. Vishwanath, and A. Yazdani, Nat. Mater. **13**, 851 (2014).
[32] Z. Wang, H. Weng, Q. Wu, X. Dai, and Z. Fang, Phys. Rev. B **88**, 125427 (2013).
[33] M. Neupane, S.-Y. Xu, R. Sankar, N. Alidoust, G. Bian, C. Liu, I. Belopolski, T.-R. Chang, H.-T. Jeng, H. Lin, A. Bansil, F. Chou, and M. Z. Hasan, Nat. Commun. **5**, 3786 (2014).
[34] S. Borisenko, Q. Gibson, D. Evtushinsky, V. Zabolotnyy, B. Büchner, and R. J. Cava, Phys. Rev. Lett. **113**, 027603 (2014).
[35] Z. K. Liu, J. Jiang, B. Zhou, Z. J. Wang, Y. Zhang, H. M. Weng, D. Prabhakaran, S.-K. Mo, H. Peng, P. Dudin, T. Kim, M. Hoesch, Z. Fang, X. Dai, Z. X. Shen, D. L. Feng, Z. Hussain, and Y. L. Chen, Nat. Mater. **13**, 677 (2014).
[36] T. Liang, Q. Gibson, M. N. Ali, M. Liu, R. J. Cava, and N. P. Ong, Nat. Mater. **14**, 280 (2015).
[37] Z. K. Liu, B. Zhou, Y. Zhang, Z. J. Wang, H. M. Weng, D. Prabhakaran, S.-K. Mo, Z. X. Shen, Z. Fang, X. Dai, Z. Hussain, and Y. L. Chen, Science **343**, 864 (2014).
[38] Z. Wang, Y. Sun, X.-Q. Chen, C. Franchini, G. Xu, H. Weng, X. Dai, and Z. Fang, Phys. Rev. B **85**, 195320 (2012).
[39] S.-Y. Xu, C. Liu, S. K. Kushwaha, T.-R. Chang, J. W. Krizan, R. Sankar, C. M. Polley, J. Adell, T. Balasubramanian, K. Miyamoto, N. Alidoust, G. Bian, M. Neupane, I. Belopolski, H.-T. Jeng, C.-Y. Huang, W.-F. Tsai, H. Lin, F. C. Chou, T. Okuda, A. Bansil, R. J. Cava, and M. Z. Hasan, arXiv:1312.7624.
[40] S.-Y. Xu, C. Liu, S. K. Kushwaha, R. Sankar, J. W. Krizan, I. Belopolski, M. Neupane, G. Bian, N. Alidoust, T.-R. Chang, H.-T. Jeng, C.-Y. Huang, W.-F. Tsai, H. Lin, P. P. Shibayev, F.-C. Chou, R. J. Cava, and M. Z. Hasan, Science **347**, 294 (2015).
[41] C.-K. Chiu and A. P. Schnyder, J. Phys: Conf. Ser. **603**, 012002 (2015).
[42] A. A. Zyuzin and A. A. Burkov, Phys. Rev. B **86**, 115133 (2012).
[43] C.-X. Liu, P. Ye, and X.-L. Qi, Phys. Rev. B **87**, 235306 (2013).
[44] S. A. Parameswaran, T. Grover, D. A. Abanin, D. A. Pesin, and A. Vishwanath, Phys. Rev. X **4**, 031035 (2014).
[45] M. M. Vazifeh and M. Franz, Phys. Rev. Lett. **111**, 027201 (2013).
[46] N. B. Kopnin, T. T. Heikkilä, and G. E. Volovik, Phys. Rev. B **83**, 220503 (2011).
[47] E. Tang and L. Fu, Nat. Phys. **10**, 964 (2014).
[48] G. Z. Magda, X. Jin, I. Hagymasi, P. Vancso, Z. Osvath, P. Nemes-Incze, C. Hwang, L. P. Biro, and L. Tapaszto, Nature (London) **514**, 608 (2014).
[49] Y. Huh, E.-G. Moon, and Y. B. Kim, Phys. Rev. B **93**, 035138 (2016).
[50] J.-W. Rhim and Y. B. Kim, Phys. Rev. B **92**, 045126 (2015).
[51] M. N. Ali, Q. D. Gibson, T. Klimczuk, and R. J. Cava, Phys. Rev. B **89**, 020505 (2014).
[52] G. Bian, T.-R. Chang, R. Sankar, S.-Y. Xu, H. Zheng, T. Neupert, C.-K. Chiu, S.-M. Huang, G. Chang, I. Belopolski, D. S. Sanchez, M. Neupane, N. Alidoust, C. Liu, B. Wang, C.-C. Lee, H.-T. Jeng, C. Zhang, Z. Yuan, S. Jia, A. Bansil, F. Chou, H. Lin, and M. Z. Hasan, Nat. Commun. **7**, 10556 (2016).
[53] G. Bian, T.-R. Chang, H. Zheng, S. Velury, S.-Y. Xu, T. Neupert, C.-K. Chiu, D. S. Sanchez, I. Belopolski, N. Alidoust, P.-J. Chen, G. Chang, A. Bansil, H.-T. Jeng, H. Lin, and M. Z. Hasan, Phys. Rev. B **93**, 121113(R) (2016).
[54] R. Yu, H. Weng, Z. Fang, X. Dai, and X. Hu, Phys. Rev. Lett. **115**, 036807 (2015).

[55] L. M. Schoop, M. N. Ali, C. Straßer, V. Duppel, S. S. P. Parkin, B. V. Lotsch, and C. R. Ast, arXiv:1509.00861.
[56] L. S. Xie, L. M. Schoop, E. M. Seibel, Q. D. Gibson, W. Xie, and R. J. Cava, APL Mater. **3**, 083602 (2015).
[57] K. Mullen, B. Uchoa, and D. T. Glatzhofer, Phys. Rev. Lett. **115**, 026403 (2015).
[58] M. Ezawa, Phys. Rev. Lett. **116**, 127202 (2016).
[59] J. C. Y. Teo, L. Fu, and C. L. Kane, Phys. Rev. B **78**, 045426 (2008).
[60] L. Fu, Phys. Rev. Lett. **106**, 106802 (2011).
[61] C.-K. Chiu, H. Yao, and S. Ryu, Phys. Rev. B **88**, 075142 (2013).
[62] T. Morimoto and A. Furusaki, Phys. Rev. B **88**, 125129 (2013).
[63] K. Shiozaki and M. Sato, Phys. Rev. B **90**, 165114 (2014).
[64] P. Blaha, K. Schwarz, G. K. Madsen, D. Kasnicka, and J. Luitz, *Wien2k, An Augmented Plane Wave + Local Orbitals Program for Calculating Crystal Properties*, edited by K. Schwarz (Techn. Universität Wien, Austria, 2001).
[65] J. P. Perdew, K. Burke, and M. Ernzerhof, Phys. Rev. Lett. **77**, 3865 (1996).
[66] L. Nordheim, Ann. Phys. **401**, 607 (1931).
[67] J. Kuneš, R. Arita, P. Wissgott, A. Toschi, H. Ikeda, and K. Held, Comput. Phys. Commun. **181**, 1888 (2010).
[68] N. Marzari, A. A. Mostofi, J. R. Yates, I. Souza, and D. Vanderbilt, Rev. Mod. Phys. **84**, 1419 (2012).
[69] M. P. L. Sancho, J. M. L. Sancho, J. M. L. Sancho, and J. Rubio, J. Phys. F **15**, 851 (1985).
[70] L. Lu, L. Fu, J. D. Joannopoulos, and M. Soljacic, Nat. Photon. **7**, 294 (2013).
[71] A. P. Schnyder and S. Ryu, Phys. Rev. B **84**, 060504 (2011).
[72] Y. Tanaka, M. Sato, and N. Nagaosa, J. Phys. Soc. Jpn. **81**, 011013 (2012).
[73] A. P. Schnyder, C. Timm, and P. M. R. Brydon, Phys. Rev. Lett. **111**, 077001 (2013).
[74] A. P. Schnyder and P. M. R. Brydon, J. Phys.: Condens. Matter **27**, 243201 (2015).
[75] P. Esquinazi, T. Heikkilä, Y. Lysogorskiy, D. Tayurskii, and G. Volovik, JETP Lett. **100**, 336 (2014).
[76] D. Vanderbilt and R. D. King-Smith, Phys. Rev. B **48**, 4442 (1993).
[77] T. L. Hughes, E. Prodan, and B. A. Bernevig, Phys. Rev. B **83**, 245132 (2011).
[78] This relation also holds if there is spin degeneracy, in which case ∂R is zero since the two spin components give opposite contribution.
[79] T. Fukui, Y. Hatsugai, and H. Suzuki, J. Phys. Soc. Jpn. **74**, 1674 (2005).
[80] S. T. Ramamurthy and T. L. Hughes, arXiv:1508.01205.
[81] L. Fu and C. L. Kane, Phys. Rev. B **76**, 045302 (2007).
[82] M. Diez, D. I. Pikulin, I. C. Fulga, and J. Tworzydło, New J. Phys. **17**, 043014 (2015).
[83] A. Yamakage, Y. Yamakawa, Y. Tanaka, and Y. Okamoto, J. Phys. Soc. Jpn. **85**, 013708 (2016).